

Mesostructured manganese oxides for efficient catalytic oxidation of CO, ethylene, and propylene at mild temperatures: Insight into the role of crystalline phases and physico-

*Original*

Mesostructured manganese oxides for efficient catalytic oxidation of CO, ethylene, and propylene at mild temperatures: Insight into the role of crystalline phases and physico-chemical properties / Grifasi, Nadia; Sartoretti, Enrico; Montesi, Daniel; Bensaid, Samir; Russo, Nunzio; Deorsola, Fabio Alessandro; Fino, Debora; Novara, Chiara; Giorgis, Fabrizio; Piumetti, Marco. - In: APPLIED CATALYSIS. B, ENVIRONMENTAL. - ISSN 0926-3373. - ELETTRONICO. - 362:(2025). [10.1016/j.apcatb.2024.124696]

*Availability:*

This version is available at: 11583/2993665 since: 2024-10-24T17:10:21Z

*Publisher:*

Elsevier

*Published*

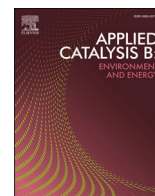
DOI:10.1016/j.apcatb.2024.124696

*Terms of use:*

This article is made available under terms and conditions as specified in the corresponding bibliographic description in the repository

*Publisher copyright*

(Article begins on next page)



# Mesostructured manganese oxides for efficient catalytic oxidation of CO, ethylene, and propylene at mild temperatures: Insight into the role of crystalline phases and physico-chemical properties

Nadia Grifasi, Enrico Sartoretti, Daniel Montesi, Samir Bensaid, Nunzio Russo, Fabio Alessandro Deorsola, Debora Fino, Chiara Novara, Fabrizio Giorgis, Marco Piumetti\*

Department of Applied Science and Technology, Polytechnic of Turin, Corso Duca Degli Abruzzi, 24, Turin 10129, Italy

## ARTICLE INFO

### Keywords:

VOCs abatement  
Indoor air purification  
Manganese oxide  
Solution combustion synthesis  
Structural defects

## ABSTRACT

Removing pollutants for indoor air purification is a key point to ensure the health and well-being of people in confined environments. This work aims to provide new insight into the development of promising manganese oxide catalysts. The effects of different crystalline phases ( $\text{MnO}_2$  and  $\text{Mn}_2\text{O}_3$ ) and the role of redox properties and structural defects were investigated to abate indoor pollutants at mild temperatures. These materials were extensively characterized through complementary techniques and catalytic tests were performed to oxidize 100 ppm of CO, ethylene, or propylene. The most promising catalyst was obtained through solution combustion synthesis, achieving total removal at 118, 222, and 172 °C, respectively, with the highest oxidation rate (2.41, 0.88, and 2.47  $\mu\text{mol g}^{-1}\text{s}^{-1}$ ) and lowest activation energy (50, 32, and 45  $\text{kJ mol}^{-1}$ ) for the three molecules. The synergy between crystalline phases enhanced the catalytic performance and their distribution in the structure was a crucial parameter affecting the number of structural defects.

## 1. Introduction

During the last decades, air purification has received extensive attention. The most common gaseous pollutants present both in outdoor and indoor spaces are Volatile Organic Compounds (VOCs); some critical features of these substances, e.g., volatility, easy diffusivity, and toxicity, can give rise to serious damage to the environment and human health [1]. Scientific studies have confirmed that indoor pollution can be more dangerous than outdoor pollution since closed and confined spaces can become “gas chambers” by retaining increasing quantities of noxious compounds (i.e., VOCs, CO, and other gaseous pollutants) [2]. As an example, EPA’s Office of Research and Development’s “Total Exposure Assessment Methodology (TEAM) Study” observed that the levels of many common organic pollutants can be 2–5 times higher inside buildings than outside [3]. Moreover, in confined spaces, such as houses, schools, offices, and so on, VOCs are emitted from many sources. Specifically, the presence of indoor VOCs is mainly due to construction materials and household products, such as paints, solvents, glue, insulating materials, furniture, wood preservatives, cleansers and disinfectants, moth repellents, and air fresheners, as well as cooking and tobacco

smoke [1,4]. Formaldehyde is one of the prevalent and toxic indoor pollutants and many efforts have been made to remove it [5–10], even if it is quite easy to oxidize. Instead, this paper considers the removal of both very common and simple substances, such as CO, and molecules more difficult to oxidize, such as ethylene and propylene, that are poorly investigated for indoor applications to the best of the author’s knowledge. For example, the removal of ethylene is quite challenging since it has C–H bonds (413  $\text{kJ mol}^{-1}$ ) and C=C bonds (615  $\text{kJ mol}^{-1}$ ), and the bond energy is higher than that of formaldehyde and carbon monoxide. This makes ethylene difficult to oxidize [11] often requiring temperatures from 200 to 300 °C. The VOCs chosen in this work could be present in closed spaces as a result of incomplete combustion during food cooking or due to cigarette smoke and also have many negative effects on human health [12,13]. In a study conducted by Jin et al. [14] in 2023, it was found that the composition of pollutants is extremely variable in libraries, canteens, dormitories, and classrooms. Generally, the majority of VOCs are generated by the combustion of a fuel, although personal care products, furniture, and paints are also classified as potential sources of VOCs [15]. For example, tobacco smoke and heating systems can play a pivotal role in producing hazardous molecules such

\* Corresponding author.

E-mail address: [marco.piumetti@polito.it](mailto:marco.piumetti@polito.it) (M. Piumetti).

<https://doi.org/10.1016/j.apcatb.2024.124696>

Received 3 May 2024; Received in revised form 28 September 2024; Accepted 11 October 2024

Available online 15 October 2024

0926-3373/© 2024 The Author(s). Published by Elsevier B.V. This is an open access article under the CC BY license (<http://creativecommons.org/licenses/by/4.0/>).

as carbon monoxide, which is particularly toxic to human health [16]. When burning incense and wax, the presence of propylene can also be detected [17]. Natural processes may produce VOCs as well: e.g., ethylene is commonly released during fruit ripening, and this substance can reach relatively high concentrations (< 2 %) in canteens [14]. In addition, outdoor pollution can be considered a sort of “secondary” source: in fact, the pollutants originating from traffic or industrial activities can enter a room through natural ventilation, mechanical ventilation, and infiltration. This can contribute to the presence of VOCs such as ethylene, propylene, benzene, etc. in confined spaces [17,18]. The effects related to altered indoor air quality (IAQ) depend on I) the type and concentration of the pollutant, II) the presence of synergies with other pollutants, III) the exposure time, and IV) the susceptibility of exposed people [2,3]. Exposure to VOCs, even for a short time, can cause a variety of direct and long-term impacts on human health, including eye, nose, and throat irritation, headaches and loss of coordination, nausea, and damage to the liver, kidneys, or central nervous system. Moreover, some VOCs are suspected of being correlated to carcinogenesis, teratogenesis, or mutagenesis in the human body [18–21].

Therefore, the emissions of VOCs into the indoor environment have started to be strictly regulated in recent years, but the existing legislation varies greatly from one country to another (see Table S1, Supporting Information). Due to the above-mentioned toxicity problems, removing pollutants for indoor air purification is a key point to ensuring the health and well-being of people in enclosed and confined environments. In this context, several technologies have been developed and explored to remove indoor pollutants, including purging, biological filtration, photocatalytic oxidation (PCO), thermal catalytic oxidization, and plasma [1,4,10,19]. However, sometimes, their employment presents some limitations, as reported in Table S2. Among all these air-cleaning technologies, catalytic oxidation at low or mild temperatures appears to be an effective and promising approach for the complete removal of indoor VOCs, due to its high economic feasibility, low cost, and ability to be operated at a lower temperature with controlled selectivity [1,4,10].

During the last decades, many researchers have focused on the use of different transition metal oxides for the catalytic oxidation of different VOCs [5–8,22–24], including manganese-based oxides [25,26], ceria-based oxides [27,28], or their mixed oxide [27,29–31]. Transition metal oxides are good alternatives to noble metals thanks to their limited cost.  $\text{MnO}_x$  catalysts have received extensive investigation, mainly thanks to their high activity, durability, low toxicity, and excellent physico-chemical properties [32]. In fact, manganese oxides can exhibit different valence states of Mn and form structural defects, resulting in significant differences in their ability to provide lattice oxygen and high oxygen mobility, which is strongly related to catalytic performance [32]. In addition, manganese oxides can be prepared through different procedures (i.e., sol-gel, reflux, hydrothermal, redox methods) and they can exhibit various crystal phases, i.e.,  $\beta\text{-MnO}_2$ ,  $\gamma\text{-MnO}_2$ ,  $\alpha\text{-Mn}_2\text{O}_3$ ,  $\gamma\text{-Mn}_2\text{O}_3$ ,  $\alpha\text{-Mn}_3\text{O}_4$ , and  $\text{Mn}_5\text{O}_8$ , affecting the catalytic performance. The same chemical composition but different structures or morphology show diverse catalytic activity for the preferential exposure of different active sites [4]. For example, Kong et al. [33] showed that  $\gamma\text{-MnO}_2$  presented more oxygen-supplying centers and higher mobile oxygen activity than  $\alpha\text{-MnO}_2$ , further indicating that  $\gamma\text{-MnO}_2$  exhibits a stronger oxygen adsorption-desorption ability. They also tested the two catalysts for the oxidation of CO, converting it at ca. 120 °C by using  $\gamma\text{-MnO}_2$ . Li et al. [34] synthesized manganese dioxide with different phase structures through a hydrothermal method and tested them for the oxidation of toluene at different temperatures. The results showed that the catalytic activity varies as follows:  $\delta\text{-MnO}_2 > \gamma\text{-MnO}_2 > \alpha\text{-MnO}_2 > \beta\text{-MnO}_2$ . They ascribed this behavior to the different degrees of redox cycling of manganese ions on the surface. In another case,  $\alpha\text{-MnO}_2$  and  $\beta\text{-MnO}_2$  nanowires/nanorods were effective catalysts for CO oxidation [35]. Finally, Figueredo et al. [26] prepared an  $\text{Mn}_2\text{O}_3$  sample by sol-gel method and tested it for the oxidation of both propylene and ethylene, demonstrating the best performance compared to CuO and  $\text{Fe}_2\text{O}_3$ .

Despite  $\text{MnO}_x$  catalysts are highly promising materials for the oxidation of many gaseous pollutants, such as CO, ethylene, and propylene, further investigations are still needed to understand which factors promote their activity at low/mild temperatures. Indeed, most of the studies carried out so far about the catalytic performances of manganese oxides have concerned high-temperature applications (e.g. removal of pollutants from combustion exhaust gases). Conversely, there is a lack of information concerning their employment on the abatement of indoor pollutants, without needing noble metals (i.e., platinum) or additional metals (such as copper or iron), and without employing a source of light or plasma. When working at low temperatures and with highly dilute mixtures (100 ppm of pollutant), the factors associated with improved catalytic performances may vary from those that are important in conventional applications (e.g. exhaust gas treatment). In fact, the performance and mechanism could be probably quite different from those of catalytic oxidation at high concentrations [4]. Based on these premises, the main aim of this work is to provide new insights into the effect of different crystal structures (mainly  $\text{MnO}_2$  and  $\text{Mn}_2\text{O}_3$ ) and how they can interact with each other, modifying their physico-chemical properties, the structural defects, the exposed active facets, and consequently leading to different catalytic activities. The pivotal role of redox properties and above all structural defects was investigated and correlated with catalytic activity for the complete oxidation of different gaseous pollutants, through simple and cost-effective noble metal-free manganese oxide catalysts.

## 2. Experimental

### 2.1. Catalysts preparation

#### 2.1.1. Materials

All the reagents employed to prepare catalysts were used directly without any further purification. Pluronic 123 (P123, poly(ethylene glycol)-poly(propylene glycol)-poly(ethylene glycol); average  $M_n \sim 5800$ ; Sigma-Aldrich); Hydrochloric acid (HCl, 37 %; Merck); Milli-Q water; 1-Butanol (ACS reagent, 99.4 %; Sigma-Aldrich); Tetraethyl orthosilicate (TEOS; Reagent grade, 98 %, Sigma-Aldrich); manganese nitrate tetrahydrate ( $\text{Mn}(\text{NO}_3)_2 \cdot 4 \text{H}_2\text{O}$ , >97 %, Merck); n-hexane (ACS reagent, 99 %, Sigma Aldrich); NaOH (Reagent grade, >98 %, Merck), Urea (ACS reagent, 99–100.5 %, Sigma-Aldrich). The commercial  $\text{MnO}_2$  and  $\text{Mn}_2\text{O}_3$  (named  $\text{MnO}_2\text{\_comm}$  and  $\text{Mn}_2\text{O}_3\text{\_comm}$ ) were also investigated for comparison purposes.

#### 2.1.2. Nanocasting procedure (NC)

Different methodologies can be employed to obtain mesoporous materials [36]. Among them, nanocasting (NC) by a templating approach is suitable for obtaining a high specific surface area, high concentrations of active oxygen species and surface  $\text{Mn}^{4+}$ , and specific crystalline phases. For the preparation of mesoporous manganese oxide through the NC procedure, KIT-6 was employed as a hard template by following protocols in the literature [37,38]. The choice was due to considerations of the final surface area of the replica that can be obtained and the size of the pores. The template was prepared first. A suitable amount of non-ionic triblock copolymer (P123) as a surfactant was dissolved in ultra-pure water (MilliQ) and stirred until a uniform solution was obtained. Afterward, 37 wt. The HCl solution was added dropwise under vigorous stirring. Subsequently, the temperature was raised to 35 °C and a certain amount of 1-butanol was added. After 1 hour, silica precursor (TEOS) was quickly added to the solution and the mixture was kept under stirring for 24 h at 35 °C. Then, the solution was transferred to a stainless-steel autoclave (Berghof) thoroughly sealed and the reaction occurred at 100 °C for 24 h. After that, the solid product was recovered via vacuum filtration, dried at 80 °C for 24 h, and calcinated at 550 °C for 6 h with a ramp of 2 °C  $\text{min}^{-1}$ . The thus prepared KIT-6 was used as the hard template for the preparation of mesoporous  $\text{MnO}_2$  [39,40]. To do this, the KIT-6 mesoporous silica was dispersed in

n-hexane and stirred at room temperature for 3 h. Subsequently, a saturated solution of  $\text{Mn}(\text{NO}_3)_2$  was added to the mixture, stirred overnight, centrifuged, and dried at room temperature until a completely dried powder was obtained. Finally, the sample was calcinated at 400 °C for 3 h with a ramp of 1 °C  $\text{min}^{-1}$ , and the obtained material was treated twice with a 2 M hot NaOH solution to remove the template, followed by washing with water several times until the pH reached neutrality and final drying at 60 °C. The absence of significant silica residues was subsequently confirmed by XPS and EDX analyses (Figure S1). The final sample was denoted  $\text{MnO}_2\text{-NC}$ .

### 2.1.3. Solution combustion synthesis (SCS)

For the preparation of manganese oxides through the SCS procedure [41,42], a suitable amount of water was employed to completely dissolve  $\text{Mn}(\text{NO}_3)_2$  under stirring at room temperature. Urea was used as fuel and added to the solution to carry out the exothermic redox reaction. The ratio between fuel and metal precursor was found to be crucial in obtaining different crystalline phases. Precisely, to obtain  $\text{Mn}_2\text{O}_3$  and  $\text{MnO}_2$ , the amount of fuel was varied to have a molar ratio equal to 1 in the former case and 0.4 in the latter. Afterward, the solution was transferred in a crucible and placed in an oven, where the calcination took place at 400 °C for 10 min with a ramp of 5 °C  $\text{min}^{-1}$ ; at the end, the powders were rinsed to remove some impurities and dried at 60 °C. The obtained samples were denoted  $\text{Mn}_2\text{O}_3\text{-SCS}$  and  $\text{MnO}_2\text{-SCS}$ , respectively.

## 2.2. Catalysts characterization

$\text{N}_2$ -physisorption at -196 °C was performed in a Micromeritics Tristar II 3020 (v1.03, Micromeritics Instrument Corp., Norcross, GA, USA) to evaluate textural properties, e.g., the Specific Surface Area (SSA,  $\text{m}^2 \text{g}^{-1}$ ), the Total Pore Volume (VTP,  $\text{cm}^3 \text{g}^{-1}$ ) and the pore diameter (Dp) of all materials. The SSA was evaluated using the Brunauer–Emmett–Teller (BET) method, whereas the VTP and Dp were evaluated using the Barrett–Joyner–Halenda (BJH) method during the desorption phase. Prior to start, the powder samples were outgassed under  $\text{N}_2$  flow at 200 °C for 2 h to remove impurities on their surface (e. g., moisture).

The crystalline structure of the samples was investigated using powder X-ray diffraction analysis (XRD). The patterns were collected with an X'Pert Philips PW3040 (Malvern Panalytical Ltd., Malvern, UK) diffractometer using  $\text{Cu K}\alpha$  radiation ( $2\theta$  range = 20°–90°; step = 0.05°  $2\theta$ ; time per step = 0.2 s). The collected diffraction peaks were analyzed according to the Powder Data File database (PDF-2004, International Centre of Diffraction Data) and the average crystallite size was evaluated using Scherrer's formula  $D = 0.9\lambda / (b \cos \theta)$ , where  $\lambda$  is the wavelength of the  $\text{Cu K}\alpha$  radiation,  $b$  is the full width at half maximum (in radians), 0.9 is the shape factor considered for spherical particles and  $\theta$  is the angle of the diffraction peaks [43].

The catalysts' reducibility was investigated by performing temperature-programmed reduction analysis ( $\text{H}_2$ -TPR) in an ALTAMIRA AMI300 Lite TPD/R/O instrument (Georgia, USA), comprising a thermal conductivity detector (TCD). Before starting, 50 mg of powder sample was placed in a quartz U-tube reactor and pretreated by flowing 20 mL  $\text{min}^{-1}$  of pure He at 400 °C for 1 h. Subsequently, after cooling to 50 °C, 20 mL  $\text{min}^{-1}$  of reducing gas mixture containing 5 vol% of  $\text{H}_2/\text{Ar}$  was fed to the sample. The temperature was monitored with a thermocouple placed in the reactor and increased from 50 °C to 700 °C with a heating rate of 5 °C  $\text{min}^{-1}$ ; the final temperature was kept for 30 min. To further confirm the transition of crystalline phases, *in-situ* XRD was performed reproducing the same procedure adopted for the  $\text{H}_2$ -TPR analysis. The powder was pretreated by flowing 20 mL  $\text{min}^{-1}$  of pure  $\text{N}_2$  at 400 °C for 1 h and, after cooling to 50 °C, 20 mL  $\text{min}^{-1}$  of reducing gas mixture containing 5 vol% of  $\text{H}_2/\text{N}_2$  was fed to the sample. The patterns were collected at the temperatures at which the reduction peaks were observed in the  $\text{H}_2$ -TPR analysis.

Oxygen temperature programmed desorption analysis ( $\text{O}_2$ -TPD) was performed with the same instrument. Prior to start, 50 mg of powder was pretreated with a 40 mL  $\text{min}^{-1}$  flow of  $\text{O}_2$  at 400 °C for 30 min. Subsequently, the temperature was cooled down to 50 °C keeping the oxygen flow. The analysis was carried out by heating the sample to 850 °C with a heating ramp of 5 °C  $\text{min}^{-1}$  under a 40 mL  $\text{min}^{-1}$  flow of He, holding the final temperature for 15 min.

Temperature-programmed desorption analysis of ammonia ( $\text{NH}_3$ -TPD) was performed with the same instrument, to investigate the role of acidity in the VOC oxidation mechanism. Prior to start, 50 mg of powder was pretreated with a 25 mL  $\text{min}^{-1}$  flow of He at 300 °C for 30 min. Subsequently, the temperature was cooled down to 100 °C, and 2500 ppm of  $\text{NH}_3$  was fed for 2 h. The analysis was carried out by heating the sample to 600 °C, with a heating ramp of 5 °C  $\text{min}^{-1}$  under a 20 mL  $\text{min}^{-1}$  flow of He, holding the final temperature for 15 min.

X-ray photoelectron spectroscopy (XPS) was used to determine the elemental composition and oxidation states of elements at the surface of the materials. All the powder samples were pressed into thin discs and the measurements were performed in a PHI 5000 Versa probe apparatus (Physical Electronics Inc. PHI, Chanhassen, MN, USA) using the following conditions: band-pass energy of 187.85 eV, a 45° take-off angle and a 100.0  $\mu\text{m}$  diameter X-ray spot size.

The morphology of the samples was studied through field emission scanning electron microscopy analysis (FESEM, Zeiss MERLIN, Gemini-II column, Oberkochen, Germany) using an extra high tension (EHT) of 3 kV, a working distance (WD) of about 3 mm and a probe intensity of 115 pA. EDX analysis was performed on the same apparatus, to check the presence of silica residues in the sample obtained through NC procedure. Moreover, the internal structure was studied through high-resolution transmission electron microscopy (HR-TEM, Talos Thermo Scientific) with a  $\text{LaB}_6$  gun, operating at 200 kV. A little powder was dispersed in pure isopropanol, sonicated for 15 minutes at room temperature, and deposited on copper grids equipped with lacey carbon films. The acquired images were processed with ImageJ software to obtain the particle size distribution.

Atomic force microscopy (AFM) was performed using a scanning probe microscope (Bruker Innova, USA) equipped with Bruker RTESPA-300 etched silicon probes with a nominal tip radius of 8 nm. For what concerns topographical analyses, catalyst tablets were prepared by compressing a little powder into a press and scanned in tapping mode with a resonance frequency of about 285 kHz and a scanning rate in the range of 0.2–0.5 Hz. Instead, analysis of the nanoparticle (NP) surface roughness was performed on isolated NPs after drop-casting of a water dispersion of the synthesized samples onto a piranha-treated (mixture of  $\text{H}_2\text{SO}_4$  and  $\text{H}_2\text{O}_2$  in a ratio 3:1) silicon dice and subsequent drying in ambient air. The Gwyddion freeware was employed for data processing and roughness evaluation. In detail, the plane inclination was adjusted by subtracting the average plane and by setting the scale zero position at the minimum value measured. The average roughness ( $R_a$  parameter) was evaluated by taking 10 differently oriented profiles on each investigated NP using a line width of 3 pixels. The surface roughness of each catalyst was finally expressed in terms of the mean value and standard deviation of the calculated  $R_a$  parameters.

To further investigate the structural properties of manganese oxides and give some elucidations about the defects present in the structure, Raman spectroscopy was performed through a Renishaw InVia micro-Raman spectrometer (Renishaw plc, Wotton-under-Edge, UK). For each sample, the spectra were collected at room temperature in five different points, to verify if the material was homogenous, using a 514.5 nm excitation wavelength, a 1 mW laser power, a 20x objective, and a 225 s total acquisition time.

### 2.3. Catalytic tests and kinetic study

Catalytic oxidation tests were performed in a fixed-bed quartz U-shaped reactor (ID = 4 mm) heated by a PID-controlled furnace. The bed

temperature was monitored by a K-type thermocouple placed into the reactor. Before starting, 50 mg of powder catalyst was pretreated under a 100 mL min<sup>-1</sup> flow of pure N<sub>2</sub> at 150 °C for 1 h, to remove the physisorbed species (i.e., moisture and other gaseous species). After the natural cooling to room temperature, 50 mL min<sup>-1</sup> of a gaseous reactive mixture simulating a real indoor atmosphere was fed into the reactor. The mixture contained the highest concentration of gaseous pollutant allowed in confined spaces, which is equal to 100 ppm of pollutant (either CO, ethylene, or propylene as probe molecules), 21 vol% of O<sub>2</sub> and N<sub>2</sub> to balance. During the test, a gas hourly space velocity (GHSV) of 47747 h<sup>-1</sup> and a catalyst weight-to-volumetric flow rate ratio (W F<sup>-1</sup>) of 1 mg min mL<sup>-1</sup> were maintained. The test started at 25 °C and subsequently, the temperature was raised with an isothermal step every 25 °C to avoid the effect of adsorption-desorption phenomena. The test finished when the pollutant conversion reached 100 %. The outlet gas composition was monitored continuously through a non-dispersive infrared (NDIR) gas analyzer ABB Uras 14 (ABB S.p.A – PAMA, Milan, Italy) connected to the outlet of the reactor. For comparison purposes, two commercial Mn-based oxide samples (namely MnO<sub>2</sub> and Mn<sub>2</sub>O<sub>3</sub>, from Sigma-Aldrich) were also investigated.

Further investigations were carried out through kinetic studies. In more detail, the catalytic oxidation of CO and VOCs was modeled with a pseudo-homogeneous first-order reaction. Since the catalytic tests were performed with a great excess of O<sub>2</sub> (21 vol%), compared to the pollutant, the influence of the former reactant is negligible on the reaction rate, and its concentration is assumed almost constant. Considering these hypotheses, the reaction rates per unit mass and square meter of catalyst were evaluated as follows:

$$r_{\text{CO/VOC}} = \frac{\dot{n}_{\text{CO/VOC}} \zeta_{\text{CO/VOC}}}{W_{\text{cat}}} \quad (1)$$

$$r^*_{\text{CO/VOC}} = \frac{r_{\text{CO/VOC}}}{\text{SSA}} \quad (2)$$

where  $r_{\text{CO/VOC}}$  is the reaction rate per unit mass of catalyst ( $\mu\text{mol s}^{-1} \text{g}^{-1}$ ),  $r^*_{\text{CO/VOC}}$  is the reaction rate per square meter of catalyst surface ( $\mu\text{mol s}^{-1} \text{m}^{-2}$ ),  $\dot{n}_{\text{CO/VOC}}$  is the inlet flowrate of pollutant ( $\mu\text{mol s}^{-1}$ ),  $\zeta_{\text{CO/VOC}}$  is the pollutant conversion at a specific temperature (-),  $W_{\text{cat}}$  is the mass of catalyst in the reactor (g), and SSA represents the specific surface area ( $\text{m}^2 \text{g}^{-1}$ ).

Finally, the apparent activation energy (named  $E_a$  from now on) was evaluated to provide a complete overview of the catalytic performance of the synthesized samples. The value of  $E_a$  was obtained by using the Arrhenius equation. When the conversion of the pollutant is lower than 30 %, it is reasonable to neglect the dependence of the reaction rate on the products, mainly CO<sub>2</sub> and H<sub>2</sub>O, and on the variation of the inlet composition. Thus, given these hypotheses, the activation energy ( $\text{kJ mol}^{-1}$ ) can be obtained from the slope of the resulting linear plot of the logarithm of the reaction rate versus  $1/T$ , as described in Eq. (3).

$$\ln r_{\text{CO/VOC}} = - \frac{E_a}{R T} + C \quad (3)$$

Moreover, the best-performing catalyst was also tested under wet conditions, by feeding a polluted gas mixture completely saturated with moisture. The procedure adopted was similar to that used under dry conditions. Finally, cyclic tests and time-on-stream (TOS) analyses were carried out to investigate the best-performing sample's stability. Precisely, 50 mg of fresh sample was pretreated under a pure N<sub>2</sub> flow at 150 °C. After natural cooling to room temperature, a polluted gas mixture with the same composition as that tested in dry conditions was sent into the reactor. The temperature was raised with a ramp of 5 °C min<sup>-1</sup> until complete oxidation of the pollutant. The whole procedure was repeated three times. After the third cycle, TOS analysis was carried out. Specifically, at the end of the last cycle, the temperature was adjusted to have 90 % conversion and it was kept constant for 8 h in order to evaluate the

stability of the catalyst. The procedure was adopted for all the three pollutants tested. To investigate the role of oxygen species and the mechanism involved, further catalytic tests were carried out on the best-performing catalyst, under an oxygen-free atmosphere. Firstly, the sample was pretreated in pure oxygen flow (10 mL min<sup>-1</sup> at 200 °C for 2 h) using the same apparatus employed to evaluate catalytic activity. After cooling down to room temperature, the excess of O<sub>2</sub> was removed with nitrogen (100 mL min<sup>-1</sup>) that was left to flow until the oxygen concentration reached 0 ppm. Finally, the pollutant (CO/N<sub>2</sub>, 2002 ppm, 50 mL min<sup>-1</sup> or VOCs/N<sub>2</sub>, 1000 ppm, 100 mL min<sup>-1</sup>) was fed on the catalyst and the concentration of CO<sub>2</sub> and CO was monitored increasing the temperature up to 700 °C.

### 3. Results and discussion

#### 3.1. Physico-chemical characterization

All the investigated samples were extensively characterized through complementary techniques. The textural properties obtained from N<sub>2</sub> physisorption performed at -196 °C were summarized in Table 1. In particular, the values of the Specific Surface Area (SSA,  $\text{m}^2 \text{g}^{-1}$ ), the Total Pore Volume (VTP,  $\text{cm}^3 \text{g}^{-1}$ ), and the average pore diameter (Dp, nm) of all materials are reported.

As a whole, catalysts prepared with different methods exhibited dissimilar textural properties. Specifically, the highest specific surface area ( $99.5 \text{ m}^2 \text{g}^{-1}$ ) was obtained by employing the nanocasting method, using KIT-6 as a hard template, which presented almost  $813 \text{ m}^2 \text{g}^{-1}$  (see Supporting information, Table S3). Moreover, as can be seen from the N<sub>2</sub> adsorption-desorption isotherms, (see Supporting information, Figure S2(A)), the silica template exhibited adsorption hystereses associated with the type IV or V, thus belonging to mesoporous materials. According to IUPAC, this loop can be ascribed to type H1, often related to porous materials consisting of well-defined cylindrical-like pore channels [44]. Furthermore, KIT-6 shows well-defined pore sizes and narrow pore size distributions of about 5.0–8.0 nm, as evidenced by Figure S2(B). MnO<sub>2</sub>\_NC sample still showed type IV adsorption hysteresis (see Figure S3(A), Supporting information), but it seemed that a bimodal pore distribution characterized the replica. Indeed, the pore system exhibited pore diameters of 4.8 nm and 13.8 nm, respectively (see Figure S4(A), Supporting information). The results agreed with the procedure adopted since nanocasting is one of the most suitable techniques employed to obtain very porous structures [37,45].

Regarding the samples obtained through the SCS method, it can be noted that the values of all parameters significantly differed from those observed in the MnO<sub>2</sub>\_NC sample. In particular, MnO<sub>2</sub>\_SCS and Mn<sub>2</sub>O<sub>3</sub>\_SCS revealed similar specific surface areas, total pore volumes, and pore diameters, as reported in Table 1. Hysteresis loops were similar to type IV, as in the previous sample (see Figure S3(A), Supporting information), but the pore size distributions were extremely different.

**Table 1**

Textural properties and crystallite size of the samples, calculated from the N<sub>2</sub> physisorption at -196 °C and XRD patterns.

Sample	SSA <sup>a</sup> [m <sup>2</sup> g <sup>-1</sup> ]	VTP <sup>b</sup> [cm <sup>3</sup> g <sup>-1</sup> ]	Dp <sup>b</sup> [nm]	Crystallite size <sup>c</sup> [nm]
MnO <sub>2</sub> _NC	99.5	0.4	13.5	4
MnO <sub>2</sub> _SCS	35.7	0.1	13.3	7
MnO <sub>2</sub> _comm	0.4	0.0	0.0	151
Mn <sub>2</sub> O <sub>3</sub> _SCS	20.1	0.1	10.2	62
Mn <sub>2</sub> O <sub>3</sub> _comm	1.5	0.0	0.0	93

<sup>a</sup> Specific surface area (SSA) evaluated according to the Brunauer–Emmett–Teller (BET) method.

<sup>b</sup> Total Pore Volume (VTP) and average pore diameter (Dp) evaluated according to the Barrett–Joyner–Halenda (BJH) method during the desorption phase.

<sup>c</sup> Crystallite size evaluated according to Scherrer's formula.

Precisely, both samples synthesized through SCS showed a bimodal pore system with a wider range of values, i.e. 3.7–17.4 nm for MnO<sub>2</sub>\_SCS and 3.6–17.6 nm for Mn<sub>2</sub>O<sub>3</sub>\_SCS (see Figure S4(B), Supporting information). These results were in agreement with the procedure adopted and with the values reported by other authors [46]. Finally, both commercial samples presented an almost non-porous structure, since the specific surface area resulted very low; the hysteresis loop (see Figure S3(B) Supporting information) might be due to interparticle voids.

The diffraction patterns of all the samples are illustrated in Fig. 1, while their crystallite size is reported in Table 1. Concerning the commercial samples, both MnO<sub>2</sub>\_comm (A) and Mn<sub>2</sub>O<sub>3</sub>\_comm (B) showed sharp peaks, highlighting the presence of a pure phase and high crystallinity. Commercial MnO<sub>2</sub> exhibited the most intense peaks located at  $2\theta = 28.66^\circ$ ,  $37.32^\circ$  and  $56.64^\circ$  which can be ascribed to (1 1 0), (1 0 1), and (2 1 1)-type planes, respectively, in accordance with the reference patterns in the PDF database (01–081–2261). Instead, commercial Mn<sub>2</sub>O<sub>3</sub> presented the most intense peak at  $2\theta = 32.86^\circ$  corresponding to (2 2 2)-type planes, in accordance with the reference patterns in the PDF database (01–071–0635 and 01–078–0390), referred to partridgeite and bixbyite ( $\alpha$ -) phases. The Mn<sub>2</sub>O<sub>3</sub>\_SCS sample exhibited well-defined peaks with high intensity located in the same positions as those present in the commercial oxide. As well as Mn<sub>2</sub>O<sub>3</sub>\_comm, the Mn<sub>2</sub>O<sub>3</sub>\_SCS sample presented both orthorhombic and cubic structures (reference patterns 01–073–1826 and 01–071–0636, respectively), ascribed to partridgeite and bixbyite ( $\alpha$ -) phases [47], with a higher amount of the latter one. However, for this sample, the presence of two other peaks of significantly lower intensity was also detected. It can be attributed to the presence of a MnO<sub>2</sub> crystalline phase with a tetragonal structure (reference pattern 01–081–2261), as evidenced by the pattern (B).

Concerning MnO<sub>2</sub> materials, it is well known that the [MnO<sub>6</sub>] octahedral unit is the basic building block for the MnO<sub>2</sub> crystalline phase. Depending on how the units are linked to each other, MnO<sub>2</sub> can form a variety of polymorphs, such as  $\alpha$ -,  $\beta$ -,  $\gamma$ - and  $\delta$ - MnO<sub>2</sub> [47–49]. Specifically, the MnO<sub>2</sub>\_SCS sample revealed peaks that were ascribed to different crystalline phases. MnO<sub>2</sub> was present as pyrolusite phase with a tetragonal structure (reference pattern 01–071–0071) ascribed to  $\beta$ -phase, and ramsdellite phase (R-) with orthorhombic structure and common bipyramidal crystal shape (reference pattern 01–082–2169). The product of the intergrowth of the elements of pyrolusite and ramsdellite is ascribed to  $\gamma$ -phase [47,50,51]. Moreover, this SCS sample exhibited a small impurity due to the presence of one single peak ascribed to the Mn<sub>2</sub>O<sub>3</sub> crystalline phase (partridgeite) with an orthorhombic structure (reference pattern 01–071–0635). MnO<sub>2</sub>\_NC was characterized by the same crystalline phases as the MnO<sub>2</sub>\_SCS sample but in different relative amounts (see Table S4, Supporting information). Precisely, the two samples showed different amounts of pyrolusite and ramsdellite (54 % and 46 % for MnO<sub>2</sub>\_NC, and 66 % and 12 % for

MnO<sub>2</sub>\_SCS, respectively). However, no Mn<sub>2</sub>O<sub>3</sub> crystalline phase was detected in the sample synthesized through NC. Moreover, both MnO<sub>2</sub>\_NC and MnO<sub>2</sub>\_SCS samples exhibited low crystallinity patterns as observed in the literature [39,42], attributed to a smaller average crystallite size. In this regard, Table 1 reported the average crystallite size evaluated using Scherrer's formula. As a whole, both commercial samples showed bigger crystal sizes compared to the other materials (151 nm and 93 nm for MnO<sub>2</sub>\_comm and Mn<sub>2</sub>O<sub>3</sub>\_comm, respectively). These values appeared in agreement with the narrow and sharp peaks in their respective diffractograms. Mn<sub>2</sub>O<sub>3</sub>\_SCS sample exhibited quite large crystallite size, slightly higher than 62 nm, whereas MnO<sub>2</sub>\_SCS and MnO<sub>2</sub>\_NC exhibited the smallest values equal to 7 and 4 nm, respectively. The morphology and the crystalline structures of the samples were further confirmed by FESEM and Raman analyses (see later).

The elemental composition (mainly, Mn and O elements) and the oxidation state of the surface species of the catalysts were investigated through X-ray photoelectron spectroscopy (XPS) measurements. The results related to the relative amount of oxygen and manganese species were summarized in Table 2, whereas O 1 s and Mn 2p XPS spectra were reported in Fig. 2.

As highlighted from the deconvolution of O 1 s core levels in Fig. 2A, all samples exhibited two different peaks. The first one belongs to the range of 529.7–530.1 eV and can be ascribed to bulk oxygen O <sub>$\beta$</sub>  (O<sup>2-</sup> species) [25,52]. The latter was located at 531.1–531.7 eV, and it was related to superficial chemisorbed oxygens, labeled as O <sub>$\alpha$</sub>  (i.e., O<sub>2</sub>, O<sup>-</sup>, OH<sup>-</sup> and carbonates species), and oxygen vacancies as previously observed in other works [25,26,53]. The relative amount of all species was reported in Table 2. As expected, the most abundant component in all samples was lattice oxygen O <sub>$\beta$</sub> . Focusing on the synthesized catalysts, O <sub>$\beta$</sub>  was present in percentages from 60.4 at% (in MnO<sub>2</sub>\_SCS) to 61.9 at% (in Mn<sub>2</sub>O<sub>3</sub>\_SCS). In contrast, the abundance of the O <sub>$\alpha$</sub>  species ranged between 38.1 at% (in Mn<sub>2</sub>O<sub>3</sub>\_SCS) and 39.6 at% (in MnO<sub>2</sub>\_SCS). This was consistent with the values reported in the literature [25,26,52]. Interestingly, the sample obtained through the SCS procedure (named MnO<sub>2</sub>\_SCS) showed a higher amount of surface oxygens O <sub>$\alpha$</sub>  compared to others, with an O <sub>$\alpha$</sub>  to O <sub>$\beta$</sub>  ratio equal to 0.7. This outcome may suggest an enhancement of the activity toward VOCs oxidation reaction since O <sub>$\alpha$</sub>  species have higher mobility than lattice oxygen O <sub>$\beta$</sub>  [52].

In Fig. 2B, the deconvolution of Mn 2p core levels was reported. Specifically, it was possible to clearly see two main peaks. The first one, at c.a. 640.7–641.8 eV binding energy (BE) range, was related to Mn 2p<sub>3/2</sub>. Whereas the other peak at higher BE, specifically at c.a. 652.5–653.6 eV, corresponds to the Mn 2p<sub>1/2</sub> peak [53]. According to the literature [25,52], an estimation of the amount of the various manganese species (i.e., Mn<sup>4+</sup> and Mn<sup>3+</sup>) can be calculated throughout the deconvolution of the Mn 2p<sub>3/2</sub> band in two peaks. For the sake of completeness, also the fitting Mn 2p<sub>1/2</sub> was reported [54]. Considering the Mn 2p<sub>3/2</sub> orbital, all the samples exhibited peaks in the range of 641.7–642.1 eV and 642.9–643.1 eV which can be ascribed to Mn<sup>3+</sup> and Mn<sup>4+</sup> species, respectively [25–27,53,55–57]. Analogous components were also found from the deconvolution of Mn 2p<sub>1/2</sub> orbital. Furthermore, MnO<sub>2</sub>\_SCS, MnO<sub>2</sub>\_NC, and MnO<sub>2</sub>\_comm samples evidenced high Mn<sup>4+</sup>/Mn<sup>3+</sup>, highlighting a huge presence of redox couples on the

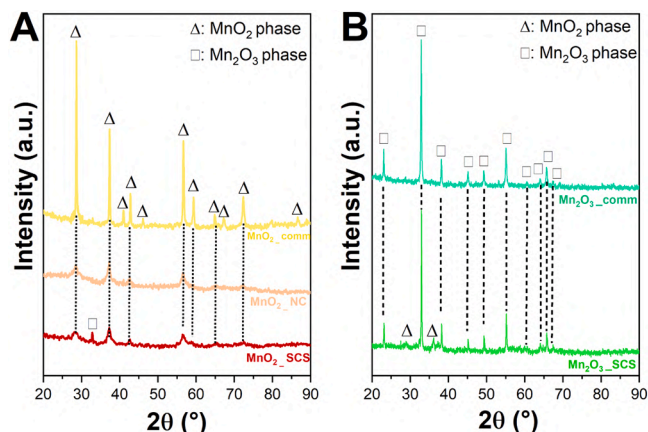


Fig. 1. X-ray diffraction patterns of MnO<sub>2</sub> samples (A) and Mn<sub>2</sub>O<sub>3</sub> samples (B).

**Table 2**  
Relative abundance of the species evaluated from the XPS spectral deconvolution.

Sample	O 1 s			Mn 2p		
	O <sub><math>\alpha</math></sub> at%	O <sub><math>\beta</math></sub> at%	O <sub><math>\alpha</math></sub> /O <sub><math>\beta</math></sub> [-]	Mn <sup>4+</sup> at%	Mn <sup>3+</sup> at%	Mn <sup>4+</sup> /Mn <sup>3+</sup> [-]
MnO <sub>2</sub> _NC	38.6	61.4	0.6	72.1	27.9	2.6
MnO <sub>2</sub> _SCS	39.6	60.4	0.7	74.2	25.8	2.9
MnO <sub>2</sub> _comm	34.6	65.4	0.5	70.4	29.6	2.4
Mn <sub>2</sub> O <sub>3</sub> _SCS	38.1	61.9	0.6	35.4	64.6	0.6
Mn <sub>2</sub> O <sub>3</sub> _comm	33.9	66.1	0.5	37.2	62.8	0.6

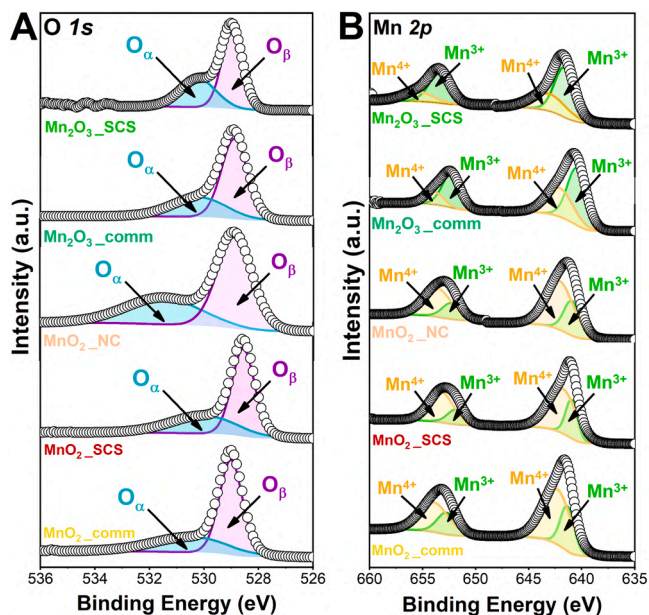


Fig. 2. XPS spectra of O 1s (A) and Mn 2p (B) core levels of the different samples.

surface, which can play an important role in catalyst performance [58–60], as discussed in Section 3.2.

The reducibility of as-prepared and commercial manganese oxides was investigated via H<sub>2</sub>-TPR and the H<sub>2</sub>-uptake profiles as a function of the temperature are plotted in Fig. 3A. The reducibility of a catalyst is an important factor that governs oxidation reactions. In general, the materials that can be reduced at lower temperatures are more active in redox processes [61]. Precisely, MnO<sub>2</sub>\_SCS, MnO<sub>2</sub>\_NC, and Mn<sub>2</sub>O<sub>3</sub>\_SCS showed reduction peaks at relatively lower temperatures, compared to the commercial oxides. Different reduction profiles were observed depending on the sample investigated. In particular, two or three peaks were present for all the catalysts, and they can be attributed to the reduction of the manganese species in different valence states [46,62]. Specifically, the synthesized samples presenting the MnO<sub>2</sub> phase exhibited two main reduction peaks: the one in the range of 270–370 °C was ascribed to the reduction of MnO<sub>2</sub> → Mn<sub>2</sub>O<sub>3</sub> or Mn<sub>2</sub>O<sub>3</sub> → Mn<sub>3</sub>O<sub>4</sub>, while the one in the range of 370–460 °C was referred to the formation of MnO [63,64]. In detail, the MnO<sub>2</sub>\_SCS sample revealed a weak shoulder at 294 °C and two intense peaks at 312 °C and 414 °C, which were ascribed to the progressive formation of crystalline phases in which manganese presented lower oxidation numbers, precisely Mn<sub>2</sub>O<sub>3</sub>, Mn<sub>3</sub>O<sub>4</sub> and MnO, in agreement with the literature [65]. The same assumptions are valid for the MnO<sub>2</sub>\_NC sample. In contrast, the commercial oxide showed one weak peak at 361 °C and a main strong peak centered at 537 °C which could be always ascribed to the formation of Mn<sub>2</sub>O<sub>3</sub>, Mn<sub>3</sub>O<sub>4</sub>, and MnO. The results were quite in line with the literature [66].

The Mn<sub>2</sub>O<sub>3</sub>\_SCS sample displayed a slightly different profile. The peak at low temperatures could be due to the presence of the MnO<sub>2</sub> crystalline phase, as highlighted in the XRD patterns. Specifically, the first weak peak centered at 280 °C can be assigned to the reactive oxygen species, as can be also observed for the sample obtained through the nanocasting procedure. The peak at 302 °C could be related to the reduction of MnO<sub>2</sub> → Mn<sub>2</sub>O<sub>3</sub>. The last peaks at 411 °C and 464 °C were ascribed to Mn<sub>2</sub>O<sub>3</sub> → Mn<sub>3</sub>O<sub>4</sub> and Mn<sub>3</sub>O<sub>4</sub> → MnO, respectively [63]. Finally, the Mn<sub>2</sub>O<sub>3</sub>\_comm sample displayed a shoulder at ca. 400 °C and a strong peak at 511 °C, which can be referred to as the formation of Mn<sub>3</sub>O<sub>4</sub> and MnO, respectively. Generally, the shift of the reduction peak position could be related to the synthesis procedure adopted [63], but also to the size of crystallites. Indeed, different synthesis procedures lead

to the formation of particles of various sizes (as estimated using Scherrer's formula, see Table 1). Larger particles seemed related to a decreased intensity of the first reduction peak and the translation of the second signal to higher temperatures. According to the literature, this could be associated with the formation of larger particles of Mn<sub>2</sub>O<sub>3</sub> which could be more resistant to reduction [67,68]. Moreover, the increased reduction temperature is linked to a decrease in the lattice oxygen mobility in the catalyst, whereas, higher reducibility means higher mobility of oxygen species [35]. The shoulder at low temperatures revealed the presence of labile oxygen species with different Mn–O strengths, in agreement with the TPD results (see later). Those species were not strongly stabilized within the oxide lattice and can be regarded as surface-reactive species [52]. Thus, it would be possible to correlate the catalytic activity of pollutant oxidation with oxygen mobility [59].

In general, the presence of shoulders and asymmetric peaks could suggest a simultaneous presence of different crystalline phases during the reduction process. To better understand this, *in-situ* XRD analyses under a reducing atmosphere were carried out and the results were reported in Fig. 3 (B–F). All the XRD patterns collected after the pre-treatment and subsequent cooling at 50 °C showed a shift of the peaks to lower angles due to the effect of the temperature on the crystal parameters. In fact, at higher temperatures, the thermal vibration of the atoms increases and provokes the expansion of the unit cell, causing a shift of 2θ positions [69–72]. Moreover, the temperature also affects the crystallinity. Precisely, it was possible to observe an increase in the intensity of the peaks, thus of the crystallinity, at higher temperatures, with a consequent increase in the average crystallite size. This effect was also observed in other materials [73,74]. For all the samples investigated, it was possible to observe the progressive change in the crystalline structure with the temperature and the reducing atmosphere following the series: MnO<sub>2</sub> → Mn<sub>2</sub>O<sub>3</sub> → Mn<sub>3</sub>O<sub>4</sub> → MnO. This was consistent with the results obtained through H<sub>2</sub>-TPR. In fact, in general, a simultaneous presence of several phases was observed. Moreover, as the temperature increased, the peaks relating to the MnO<sub>2</sub> phase decreased and those relating to the Mn<sub>2</sub>O<sub>3</sub> and Mn<sub>3</sub>O<sub>4</sub> phases appeared. At high temperatures, a further stage of reduction was observed, with the formation of MnO, which became the most stable phase. In general, it can be stated that for all samples containing MnO<sub>2</sub> in the crystalline structure, the peaks relating to this phase disappeared when the temperature was close to 300 °C, thus concluding that the first peak of the TPR profiles can be ascribed to the complete reduction of MnO<sub>2</sub> to Mn<sub>2</sub>O<sub>3</sub> or Mn<sub>3</sub>O<sub>4</sub>. At the same time, in all cases, the last peak observable on the TPR graph can be ascribed to the formation of MnO.

Furthermore, H<sub>2</sub> consumption during TPR was evaluated for all the samples. The results in terms of total H<sub>2</sub>-uptake and for each single peak were reported in Table S5 and they are in good agreement with the theoretical H<sub>2</sub> consumptions (6.33 mmol g<sup>-1</sup> for Mn<sub>2</sub>O<sub>3</sub> and 11.50 mmol g<sup>-1</sup> for the MnO<sub>2</sub>). Actually, for Mn<sub>2</sub>O<sub>3</sub>\_SCS and Mn<sub>2</sub>O<sub>3</sub>\_comm samples, a slightly higher H<sub>2</sub>-uptake was calculated, equal to 6.6 and 7.4 mmol g<sub>cat</sub><sup>-1</sup> respectively. This could be probably due to the presence of a small amount of Mn<sup>4+</sup>, as detected from other characterizations. Concerning the samples containing MnO<sub>2</sub> as the prevalent phase, both MnO<sub>2</sub>\_NC and MnO<sub>2</sub>\_comm presented an H<sub>2</sub> consumption lower than the theoretical value, whereas MnO<sub>2</sub>\_SCS exhibited a slightly higher amount. By comparing the H<sub>2</sub> uptake at low temperatures, it was noted that MnO<sub>2</sub>\_SCS exhibited the highest consumption of H<sub>2</sub> compared to the other catalysts. Precisely, at temperatures below 350 °C, this sample evidenced a consumption of 8.3 mmol g<sub>cat</sub><sup>-1</sup>, which is the highest among all the samples, thus showing a greater tendency to reduce. In contrast, both commercial samples presented quite low hydrogen consumption below 350 °C, thus demonstrating lower reducibility and, therefore, lower mobility of oxygen species. It is also known that smaller H<sub>2</sub> consumption means a lower average oxidation state (AOS), indicating that a higher amount of Mn<sup>3+</sup> could be present [75]. To validate this assumption, the oxygen-to-manganese ratios were determined from the TPR profiles and used to evaluate the average

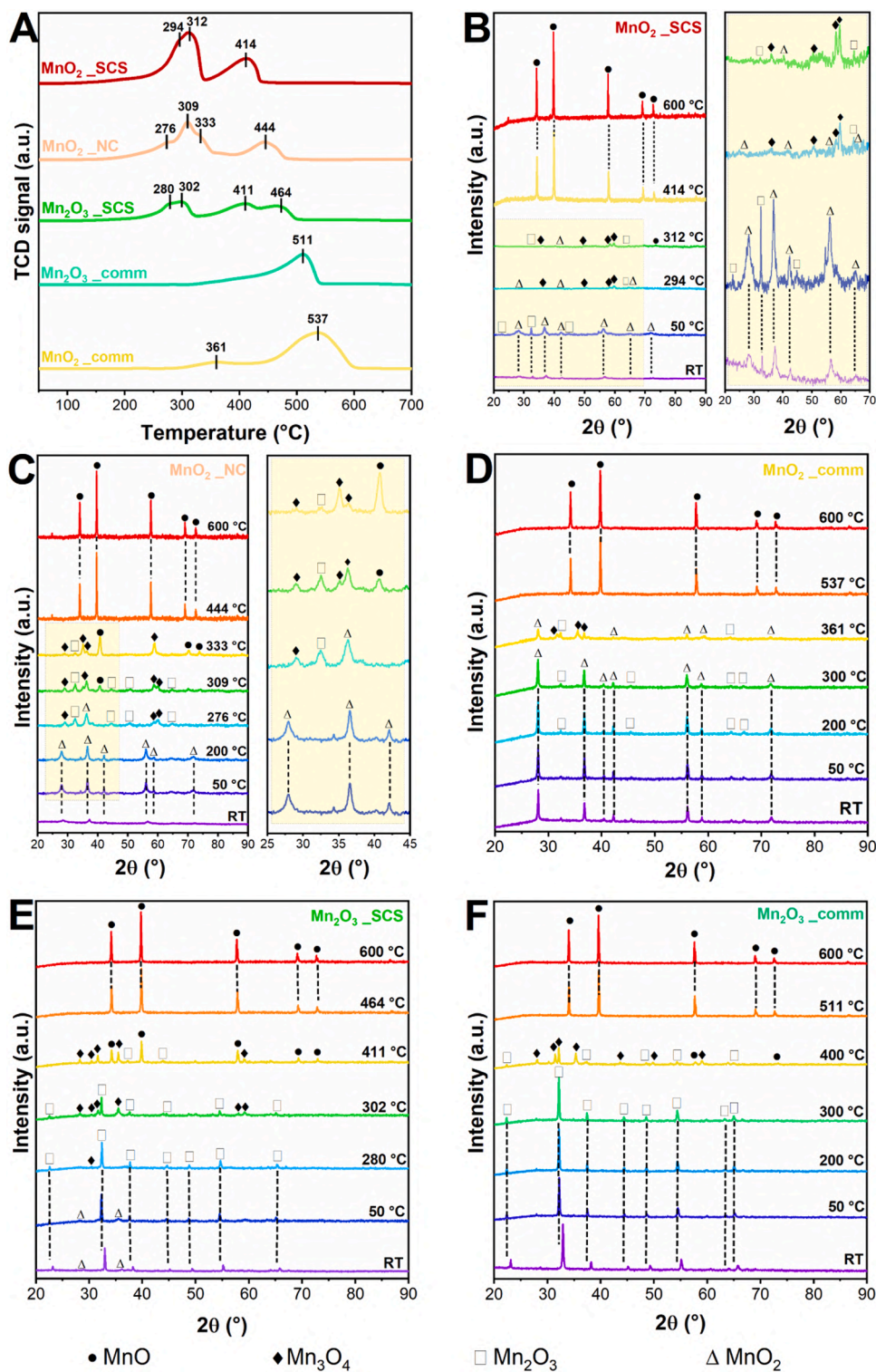


Fig. 3. H<sub>2</sub>-TPR profiles as a function of the temperature of all samples (A) and *in-situ* XRD patterns collected by flowing 20 mL min<sup>-1</sup> of 5% H<sub>2</sub>/Ar at different temperatures (B-F).

oxidation state. These values were subsequently compared to those obtained from the Mn 3s orbital. For the sake of brevity, the AOS values from the TPR and XPS are reported in Table S5. As a whole, the results are extremely in agreement with each other and close to the theoretical oxidation states. Moreover, they are consistent with the main phases detected from the XRD analysis and with the Mn<sup>4+</sup>/Mn<sup>3+</sup> ratio evaluated from XPS. The small deviations from the theoretical values could be ascribed to some impurities or secondary phases present in the samples,

in addition to the experimental error.

The properties of the oxygen species, in particular their reactivity, were investigated through O<sub>2</sub>-TPD, and the profiles are reported in Fig. 4.

As a whole, as happened for the H<sub>2</sub>-TPR, all the samples revealed quite different profiles, because of the presence of different manganese species (mainly Mn(III) and Mn(IV)) [52]. The O<sub>2</sub>-TPD pattern could be separated into three regions: surface active oxygen (< 260 °C),

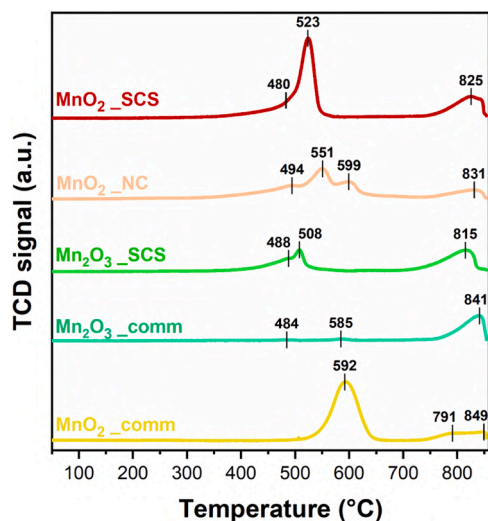


Fig. 4. O<sub>2</sub>-TPD profiles as a function of the temperature of all samples.

sub-surface lattice oxygen (260 °C–600 °C), and bulk lattice oxygen (> 600 °C), respectively [76]. It is well known that manganese oxides exhibit three types of oxygen species, according to their peak positions [52]: the  $\alpha$ -species, which are weakly bound to the surface (usually O<sub>2</sub><sup>-</sup>

and O<sup>-</sup> surface oxygen species), and the  $\beta$  and  $\gamma$  species, which are ascribed to lattice oxygen. The last two species differ from each other due to different binding strengths between manganese and oxygen. Specifically, the oxygen atoms bound to Mn(III) highlight weaker interaction, thus they are released at middle temperature during TPD; instead, the oxygen atoms bound to Mn(IV) are released at higher temperatures, and are assigned as  $\gamma$  species [52]. This is due to the fact that in the framework, the distance between O and Mn<sup>3+</sup> is larger than that between O and Mn<sup>4+</sup>, resulting in a weaker bond that facilitates desorption. Concerning the samples investigated in this work, none of them exhibited peaks below 200 °C, which could be ascribed to the desorption of weakly physically adsorbed oxygen. However, it was observed that within that range, oxygen begins to desorb, indicating that the samples start to exhibit oxygen mobility. The majority of the oxygen species in all samples can be ascribed to lattice oxygen, in agreement with other authors [52,77]. Instead, all catalysts exhibited peaks in the range of 400 °C - 600 °C, related to surface lattice oxygen desorption [33]. Precisely, the MnO<sub>2</sub>SCS sample exhibited its most intense peak at 523 °C, ascribed to lattice oxygen, with a shoulder at lower temperature referred to the desorption of surface oxygen species (O<sup>-</sup> and O<sub>2</sub><sup>-</sup>) and/or the presence of labile oxygen species ( $\beta$  species). Moreover, the peak position of the O<sub>2</sub>-TPD profile provides the activity of oxygen-supplying centers, and the integral area of the peak reveals the amounts of oxygen-supplying centers (see Table S6). It was noteworthy that the MnO<sub>2</sub>SCS sample presented more oxygen-supplying centers and higher

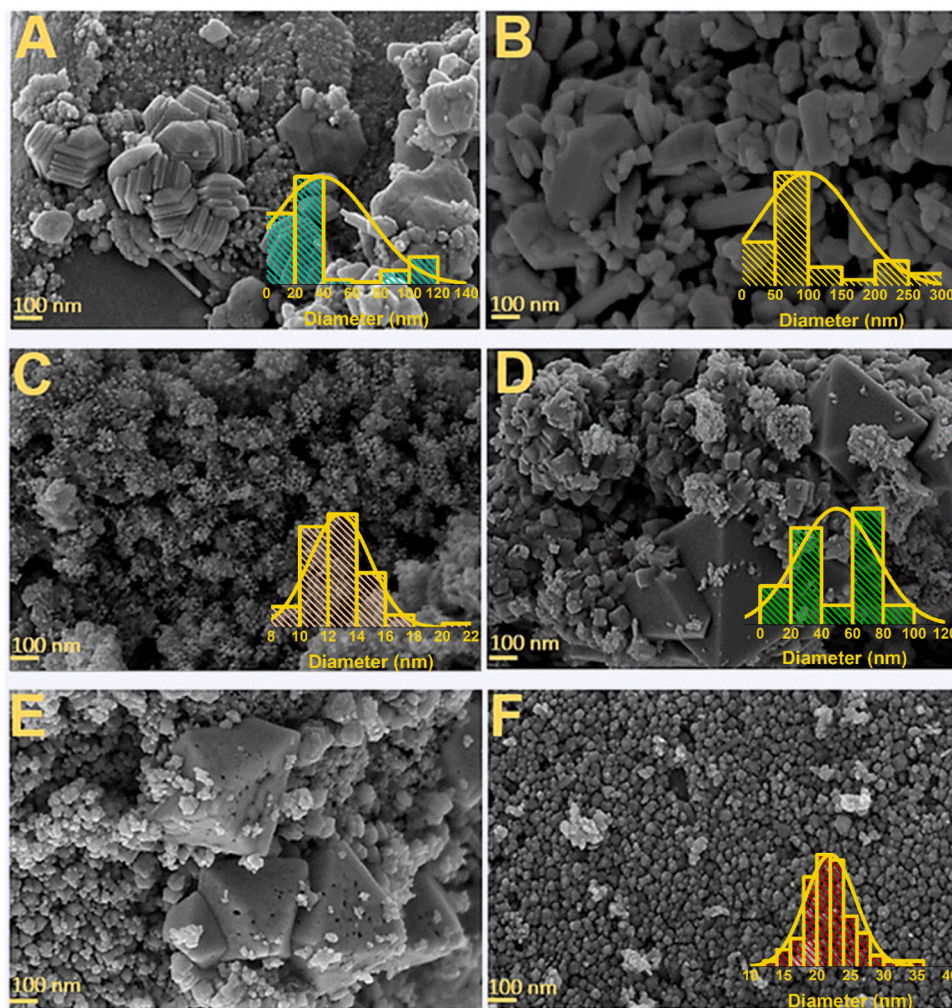


Fig. 5. FESEM representative images of the fresh powder catalysts at high magnification: Mn<sub>2</sub>O<sub>3</sub>comm (A), MnO<sub>2</sub>comm (B), MnO<sub>2</sub>NC (C), Mn<sub>2</sub>O<sub>3</sub>SCS (D), MnO<sub>2</sub>SCS (E, F).

mobile oxygen activity compared to all the other samples. Therefore, these properties may improve the catalytic performance of oxidation reactions. It has been surmised that the structure of the catalyst is responsible for the amount of oxygen that can be exploited for the reaction [68]. In this case, the abovementioned results indicated that the  $\text{MnO}_2$ \_SCS sample could provide more mobile and active surface oxygen species to participate in the catalytic reaction compared to the other materials, likely leading to better catalytic performance for pollutant oxidation [78].

The morphology of the samples was investigated through FESEM analyses, and some images were reported in Fig. 5. The commercial  $\text{Mn}_2\text{O}_3$  (Fig. 5A) sample showed a very heterogeneous morphology, with the presence of hexagonal-type and stratified structures, attributable to the presence of partridgeite phase (with orthorhombic structure). It was also possible to distinguish spherical-cubic particles ascribed to the presence of cubic phase bixbyite.  $\text{MnO}_2$ \_comm (Fig. 5B) was strikingly different since it exhibited both a rod-like morphology with well-defined and smooth surfaces and a collection of ill-defined particulate aggregates. The surfaces of these aggregates were uneven and comprised of multiple small particles, some of those spherical, ascribable to pyrolusite.  $\text{MnO}_2$ \_NC (Fig. 5C) showed interconnected nanostructures which were originated from the replication of interconnected channels in the KIT-6 template and highlighted a sort of cage/bowl-like morphologies [79]. Furthermore, the FESEM investigation allowed to identify a 3D crumbled sponge with an extremely porous structure. The morphology obtained was fairly comparable to the template structure preserved after the replication process but showed structural differences due to the expansion of the precursor within the pores of the template and its removal by the etching process [80].

The  $\text{Mn}_2\text{O}_3$ \_SCS sample (Fig. 5D) and  $\text{MnO}_2$ \_SCS sample (Fig. 5E) evidenced very interesting and unique morphology. In both cases, rhombus-like polyhedrons were recognized, precisely with bipyramidal shape well-crystallized in the octahedron, ascribed to the presence of orthorhombic phases (partridgeite and ramsdellite). These structures appeared with well-defined facets, smooth surfaces, and straight edges. Yu et al. [81] also observed this type of structure but with less defined features. Furthermore, in the case of  $\text{MnO}_2$ \_SCS, holes appeared evident on the surface of the pyramids. This can be attributed to the method of synthesis, in particular, it may be due to the reaction with fuel (urea), whose products came out of the structure during the redox reaction, causing holes that contributed to the final porosity of the material. This was not visible in the  $\text{Mn}_2\text{O}_3$ \_SCS sample probably due to the excess fuel used during the synthesis. Moreover, the  $\text{MnO}_2$ \_SCS sample (Fig. 5F) exhibited much more the presence of spherical particles with a size lower than 50 nm in diameter and with a rough surface, related to the presence of the pyrolusite phase. No excessive aggregates were observed, and clear interparticle boundaries were present. This was consistent with the literature [82] and the semi-quantitative phase estimation from XRD.

The synthesized catalysts were analyzed by atomic force microscopy (AFM) to gain further insight into the 3D topography and surface roughness. AFM images acquired on catalyst tablets were reported in

Fig. 6. AFM analyses on the  $\text{MnO}_2$ \_SCS sample (Fig. 6A) further confirmed the prevalence of rounded particles characterized by quite uniform particle size, together with the occurrence of rod-shaped nanostructures. Instead, the richness in particles featured by flat surfaces and their heterogeneous size in the  $\text{Mn}_2\text{O}_3$ \_SCS catalyst seemed to foster the formation of aggregates with reduced inter-particle porosity, as shown by the increased compaction between particles highlighted by the AFM maps reported in Fig. 6B. In agreement with the other characterization techniques, AFM revealed a very small NP size for the  $\text{MnO}_2$  catalyst obtained by the nanocasting procedure (Fig. 6C). AFM was further exploited to evaluate differences in the surface roughness among the different catalysts to explore possible correlations of this parameter with the abundance of surface defects and adsorption sites and thus with the catalytic activity. The average roughness was thus computed from high-resolution AFM images of isolated NPs for the  $\text{MnO}_2$ \_SCS and  $\text{Mn}_2\text{O}_3$ \_SCS samples ( $\text{MnO}_2$ \_NC was excluded due to the very small size of the particles which makes the analysis unreliable). Representative images of isolated NPs of the two catalysts are shown in Figure S5, while a summary of the roughness analyses is provided in Table S7. Despite the intrinsic challenges of roughness evaluation on nanosized objects, which was previously reported only by a few works [83,84], repeated measurements showed good reproducibility independently of the selected profiles used for roughness calculation. The average roughness resulted in the order of 1 nanometer for both catalysts. Thus, possible differences in the catalytic activity of the two samples should not depend on single-particle surface roughness in this case.

Furthermore, to better investigate the internal structure of the samples, TEM analysis was performed. Fig. 7 shows the internal structure of  $\text{MnO}_2$ \_SCS at two different magnifications. In Fig. 7A, it was possible to distinguish spherical and pyramidal shapes as also detected with FESEM analyses. The FFT image revealed lattice fringes with different orientations and interplanar distances. Specifically, it was possible to identify interplanar distances of 0.310 nm, 0.240 nm, and 0.322 nm, ascribed to  $\beta$ - $\text{MnO}_2$  (1 1 0),  $\beta$ - $\text{MnO}_2$  (1 0 1) and R- $\text{MnO}_2$  (2 1 0). This was also consistent with the results of XRD analyses. Moreover, it was noteworthy to observe the presence of a regular architecture that may have originated from the aligned Mn atoms in the crystal lattice, as revealed at higher magnifications (Fig. 7B).  $\text{MnO}_2$ \_NC exhibited the same facets as  $\text{MnO}_2$ \_SCS, as reported in Fig. 7C. However, depending on the percentage of the crystalline phases, additional facets were exposed. Furthermore,  $\text{MnO}_2$ \_SCS exposed (2 2 2) crystal facets due to the presence of  $\text{Mn}_2\text{O}_3$  as an impurity, as revealed from XRD analysis. This facet was also the most preferential exposed in the  $\text{Mn}_2\text{O}_3$ \_SCS sample, as reported in Fig. 7D. In some cases, it is reported that the simultaneous presence of different phases can improve catalytic performance [4,52]. In fact, structural defects originating from lattice distortion could be found in the proximity of dual-phase interfaces, which could stimulate the generation and activity of oxygen species [85].

It is also useful to point out, from AFM and FESEM analyses, that all the samples presented very different morphologies from an external point of view. If the internal constructions are considered, however, it is possible to identify further structural differences depending on how the

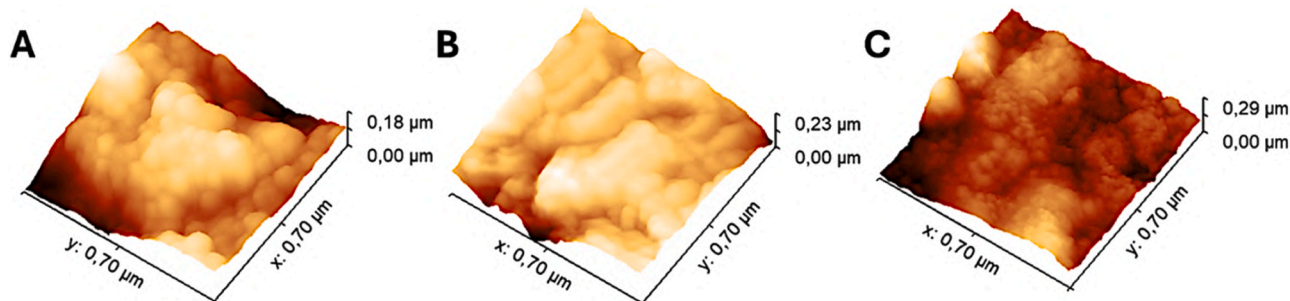


Fig. 6. AFM images of the  $\text{MnO}_2$ \_SCS (A),  $\text{Mn}_2\text{O}_3$ \_SCS (B), and  $\text{MnO}_2$ \_NC (C) fresh catalysts.

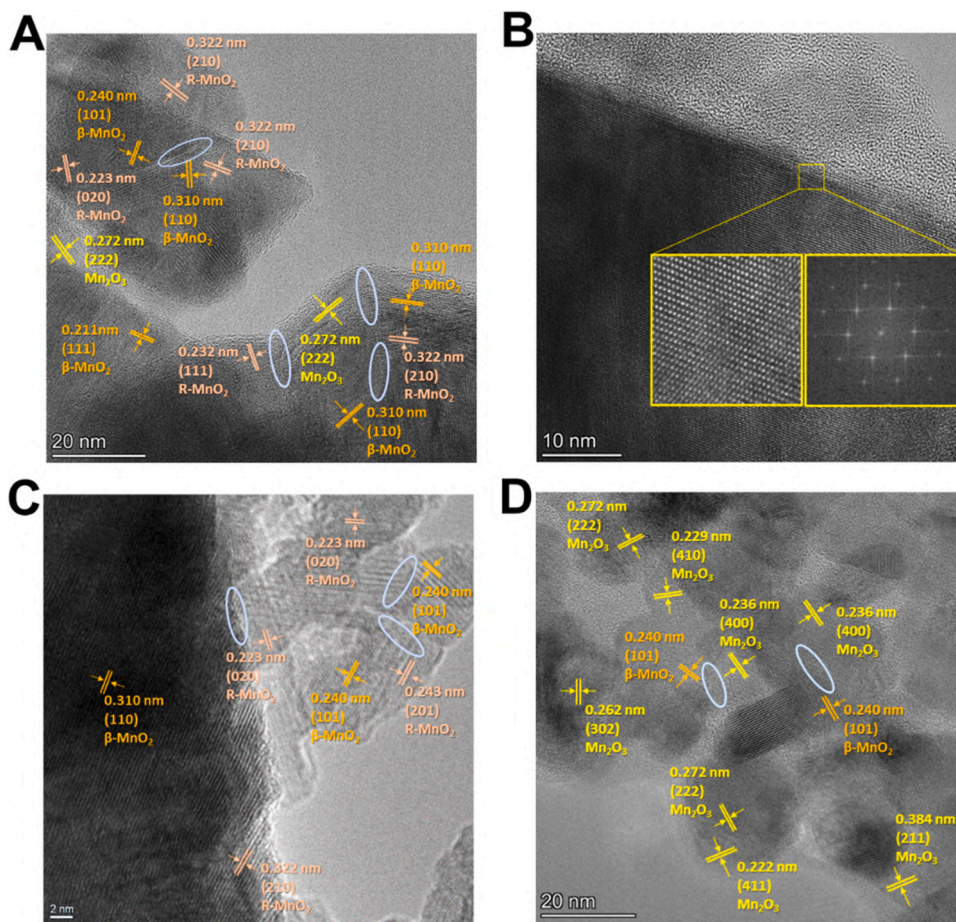


Fig. 7. HR-TEM images of MnO<sub>2</sub>\_SCS (A, B), MnO<sub>2</sub>\_NC (C), and Mn<sub>2</sub>O<sub>3</sub>\_SCS (D). The blue ellipses highlight the presence of structural defects at the dual-phase interface.

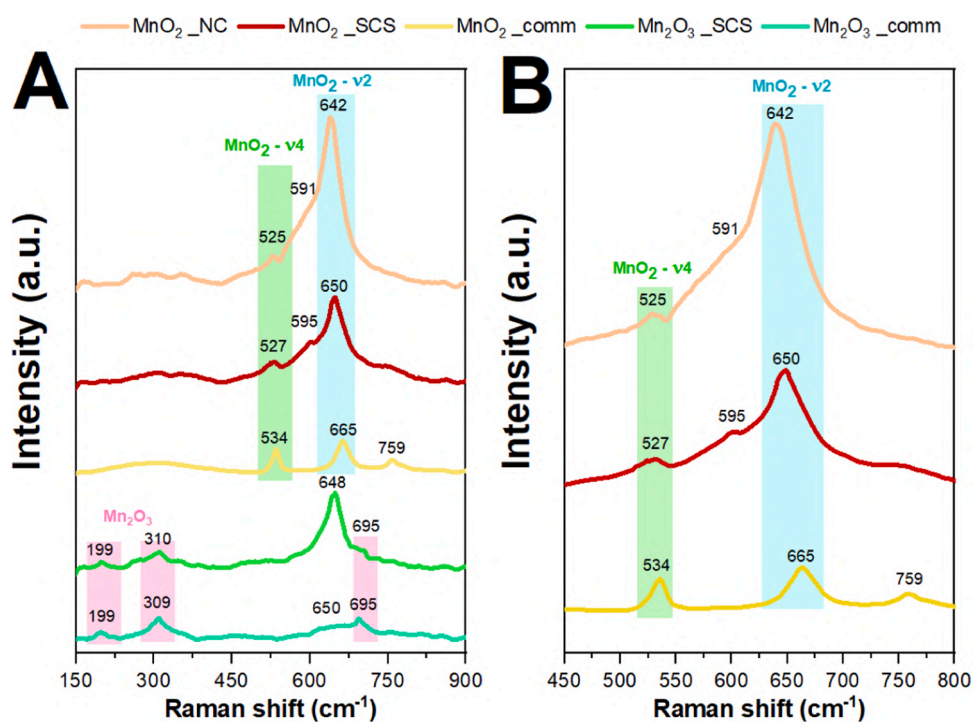


Fig. 8. Raman spectra of all samples collected at room temperature using 514.5 nm excitation wavelength (A) and the magnification of peak shift for MnO<sub>2</sub> samples (B).

[MnO<sub>6</sub>] unit shares different edges and corners to form different tunnels or layers [86].

Based on this, MnO<sub>2</sub> can build 1D, 2D, or 3D tunnel structures. From the literature [46,71,87–89], pyrolusite and ramsdellite usually show 1D features, such as (1 × 1) and (2 × 1) tunnels, whereas more complex structures (i.e., Mn<sub>2</sub>O<sub>3</sub>) belong to the 3D family. Considering the crystalline phases detected by TEM and XRD analyses, it was possible to assume that MnO<sub>2</sub>comm belongs to the 1D group since only β-phase was detected. Concerning MnO<sub>2</sub>SCS, both β- and R- phases were detected, resulting prevalently in 1D tunnel structures, with small 3D domains due to the presence of the Mn<sub>2</sub>O<sub>3</sub> phase as an impurity. Finally, MnO<sub>2</sub>NC was assumed to present a 3D structure due to the synthesis procedure adopted. In fact, using KIT-6 with interconnected pores as a hard template, also the replica presented a 3D structure, as confirmed by TEM images [64,90].

Fig. 8 shows the Raman spectra, providing interesting information about the crystalline phases and the defects present in the structures of the different samples investigated. It is well known that materials that possess γ-MnO<sub>2</sub> as crystalline phase show a peculiar structure that can be represented as an intergrowth of pyrolusite (β-MnO<sub>2</sub>) in the ramsdellite matrix (R-MnO<sub>2</sub>) [49,91,92]; a schematic representation of this structure was reported in Fig. 9. The presence of intergrowth defects, known as De Wolff structural defects, alters the structural properties, thus making the material highly promising in terms of catalytic applications. From the Raman spectra, it was possible to estimate the relationship between the position of certain peaks and the abundance of De Wolff structural defects [92]. Specifically, all the spectra exhibited strong peaks in the region between 640 and 665 cm<sup>-1</sup> ascribed to the ν<sub>2</sub> symmetric stretching of Mn-O bonds. At the same time, both Mn<sub>2</sub>O<sub>3</sub> samples also presented weak bands in the range from 199 to 360 cm<sup>-1</sup> ascribed to Mn-O bending vibrations [92,93]. Precisely, MnO<sub>2</sub>NC exhibited the most intense Raman peak at 642 cm<sup>-1</sup>, ascribed to the ν<sub>2</sub> mode, and another one with weaker intensity located at 525 cm<sup>-1</sup> referred to ν<sub>4</sub> mode (stretching). The position of the peaks related to MnO<sub>2</sub>SCS differed from the previous sample due to the percentage of pyrolusite phase present in the structure, as detected from the XRD analysis, and also due to the abundant oxygen vacancies in the MnO<sub>2</sub> lattice [94], as demonstrated from O<sub>2</sub>-TPD analysis. Specifically, since the percentage of β-phase was higher compared to MnO<sub>2</sub>NC (see Supporting information, Table S4), it was possible to observe a shift of the wavenumber of the ν<sub>2</sub> and ν<sub>4</sub> modes to higher values, specifically 650 cm<sup>-1</sup> and 527 cm<sup>-1</sup>, respectively, that are closer to those of the pure β-phase than R-phase. In addition, it can be seen that the main peak of the MnO<sub>2</sub>NC sample was more pronounced than that of the MnO<sub>2</sub>SCS sample. This can be attributed to a different crystallinity of the structure due to

different synthesis procedures employed. Indeed, the narrower and sharper peak indicates the increase in the ordered arrangement of the MnO<sub>2</sub> lattice [60,93]. For the commercial sample MnO<sub>2</sub>comm, the blueshift was even more evident, and the positions of the peaks coincided exactly with those of the pure pyrolusite phase, i.e. 665 and 534 cm<sup>-1</sup> for ν<sub>2</sub> and ν<sub>4</sub> modes, respectively. Finally, all three MnO<sub>2</sub> samples showed a weak peak localized around 591–595 cm<sup>-1</sup> that can be ascribed to a stretching mode and remained almost constant despite the percentage of pyrolusite, in line with the literature [49,92]. Finally, Mn<sub>2</sub>O<sub>3</sub>SCS and Mn<sub>2</sub>O<sub>3</sub>comm showed almost the same positions of the peaks located in the range 500–750 cm<sup>-1</sup>, ascribed to the Mn-O stretching modes [49]; these components, centered at 648 and 695 cm<sup>-1</sup> for the former sample and 650 and 695 cm<sup>-1</sup> for the latter, are characteristic of the presence of Mn<sub>2</sub>O<sub>3</sub> as main crystalline phase and agree with the literature [49,95–98]. For the Mn<sub>2</sub>O<sub>3</sub>SCS sample, the presence of a much more intense peak at 648 instead of 695 cm<sup>-1</sup> may be due to the presence of a small percentage of MnO<sub>2</sub> in the structure, as also detected by XRD; since this MnO<sub>2</sub> Raman signal is relatively more intense, as can be seen for the samples described above, it overlaps with the profile of Mn<sub>2</sub>O<sub>3</sub>.

### 3.2. Catalytic activity under dry conditions, wet conditions and stability test

Fig. 10 illustrates the results of the catalytic tests, in terms of conversion curves as a function of the temperature. As evidenced, the catalytic activity of manganese oxides was highly dependent on the preparation method and crystalline phase. Interestingly, the catalytic performances of all synthesized catalysts (MnO<sub>2</sub>SCS, MnO<sub>2</sub>NC, and Mn<sub>2</sub>O<sub>3</sub>SCS) were noteworthy, since the amount of each sample in the reactor was lower than that used in other works (50 mg compared to 100 mg or more) [99]. As a whole, for CO, ethylene, and propylene oxidation, the best-performing catalyst was MnO<sub>2</sub>SCS, exhibiting an oxidation activity already at 50 °C and 100 °C for CO and VOCs, respectively, and showing complete removal of the pollutants at 118 °C, 222 °C and 172 °C for CO, ethylene, and propylene, respectively. Table 3 reported the values of T10, T50, and T90, which correspond to the temperatures at which the conversion reached 10 %, 50 % and 90 %. It was interesting to observe that MnO<sub>2</sub>NC and Mn<sub>2</sub>O<sub>3</sub>SCS showed similar values for the oxidation of both VOCs, whereas in the case of CO, the nanocasting sample evidenced slightly better results. However, MnO<sub>2</sub>SCS exhibited the best performance in each case, reaching T10, T50, and T90 equal to 54 °C, 83 °C and 99 °C for CO oxidation, 119 °C, 169 °C and 209 °C for the ethylene oxidation and 102 °C, 134 °C and 163 °C for the propylene oxidation.

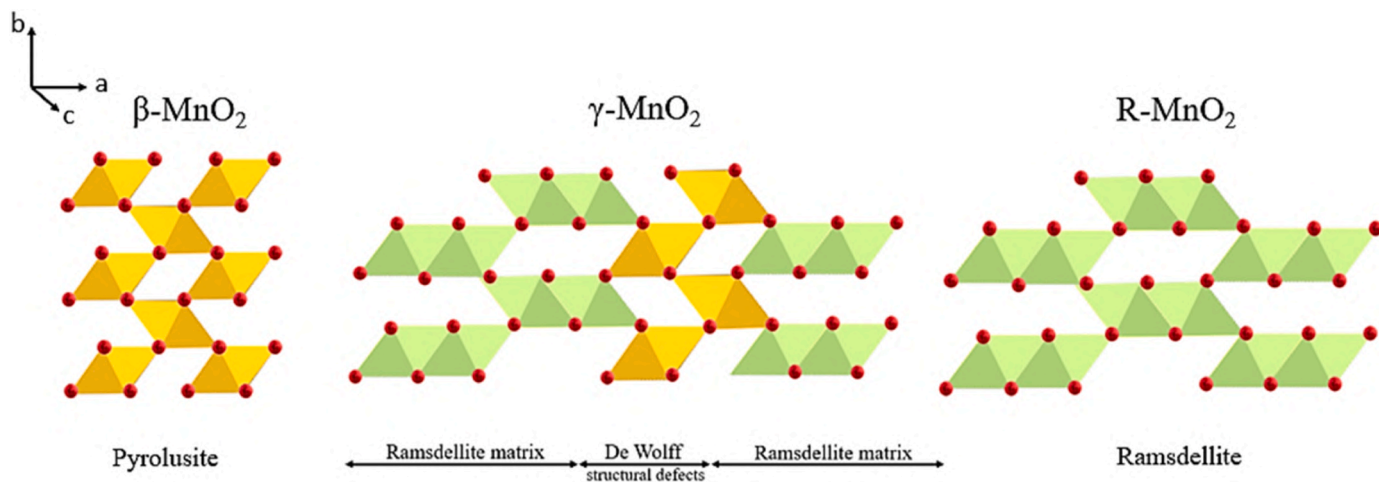


Fig. 9. Schematic representation of γ-MnO<sub>2</sub> obtained from the intergrowth of pyrolusite block (De Wolff defects) into ramsdellite matrix. Image adapted from [91] with modifications.

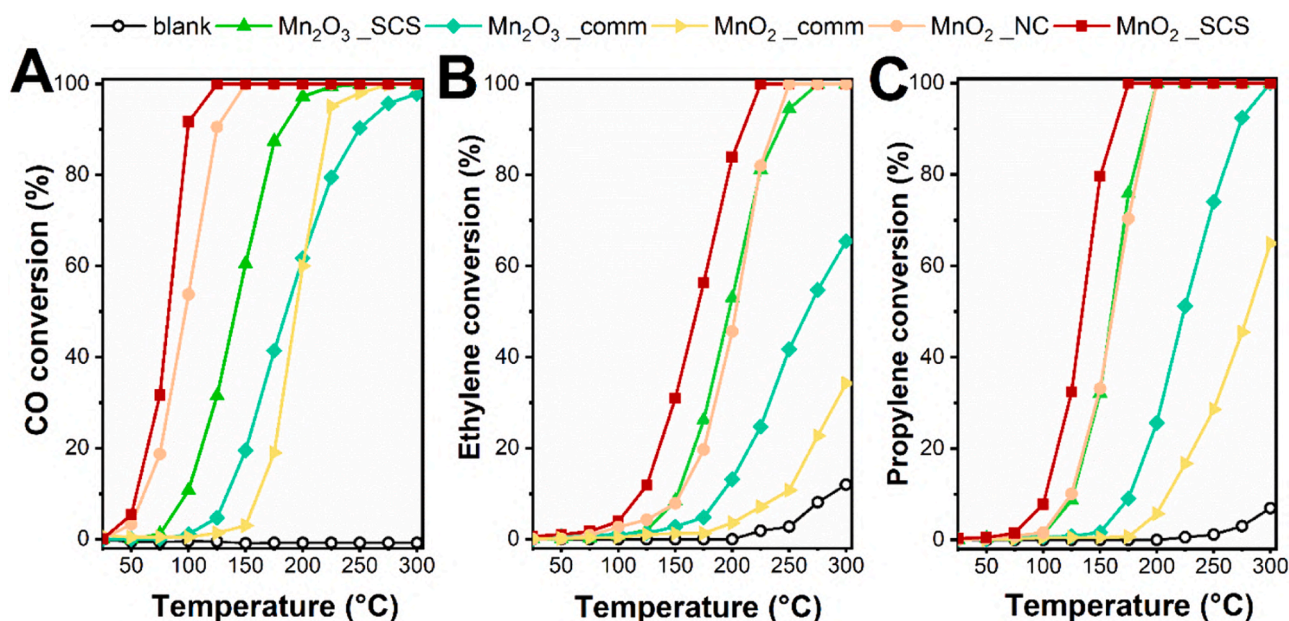


Fig. 10. Catalytic conversion of CO (A), ethylene (B), and propylene (C) as a function of the temperature in dry conditions, feeding gaseous mixture with 100 ppm of pollutant, 21 vol% O<sub>2</sub> and N<sub>2</sub> to balance over 50 mg of catalyst.

Table 3  
Values of T10, T50, and T90 evaluated for CO, ethylene, and propylene oxidation over catalysts.

Sample	CO			Ethylene			Propylene		
	T <sub>10</sub> [°C]	T <sub>50</sub> [°C]	T <sub>90</sub> [°C]	T <sub>10</sub> [°C]	T <sub>50</sub> [°C]	T <sub>90</sub> [°C]	T <sub>10</sub> [°C]	T <sub>50</sub> [°C]	T <sub>90</sub> [°C]
MnO <sub>2</sub> _NC	61	97	125	154	203	236	125	161	192
MnO <sub>2</sub> _SCS	54	83	99	119	169	209	102	134	163
MnO <sub>2</sub> _comm	161	194	221	245	>300	>300	210	281	>300
Mn <sub>2</sub> O <sub>3</sub> _SCS	98	141	182	152	197	242	126	160	190
Mn <sub>2</sub> O <sub>3</sub> _comm	134	186	249	190	266	>300	176	224	272

Furthermore, the most performing catalyst (MnO<sub>2</sub>\_SCS) was also tested under wet conditions, by feeding a mixture completely saturated with moisture, keeping the same concentration of pollutant and oxygen.

The results are displayed in Fig. 11 and the conversion rates are reported in Table 6.

As expected, the presence of moisture in the inlet mixture worsened

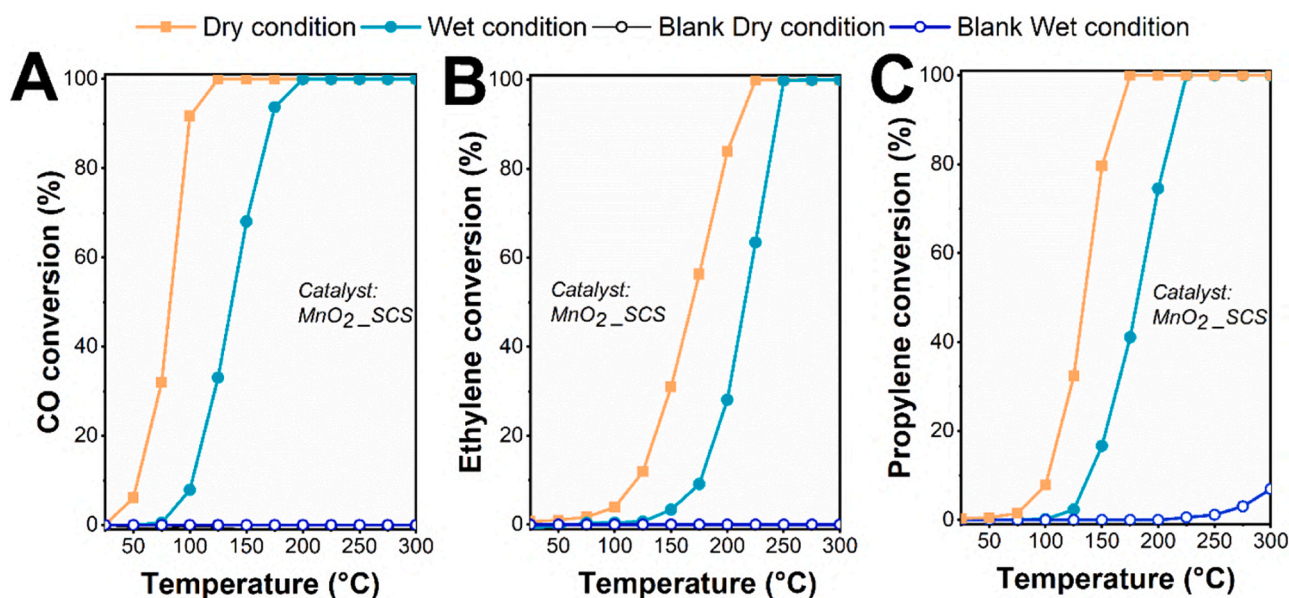


Fig. 11. Catalytic conversion of CO (A), ethylene (B), and propylene (C) as a function of the temperature in wet conditions, feeding gaseous mixture completely saturated with moisture containing 100 ppm of pollutant, 21 vol% O<sub>2</sub>, and N<sub>2</sub> to balance over 50 mg of catalyst.

the performance, since at low temperatures there could be competitive adsorption between water and pollutant on the same active site, as demonstrated in other works [29,100]. Since the surface oxygen species are not fully coordinated, they tend to attract protons to neutralize the charge; in the presence of moisture in the reactant stream, the hydrogen in the water tends to make hydrogen bonds with these surface oxygens [101], thus competing with the CO or VOC molecules. Therefore, the adsorption of moisture on the catalysts' surface can block the active sites, hindering the CO and VOC oxidation. However,  $\text{MnO}_2\text{-SCS}$  still showed good removal capability toward CO and VOCs, even if the conversion rates were slower than dry conditions for all pollutants tested (see Table 6).

To further investigate the performance of the best catalyst, three consecutive runs of catalytic oxidation were carried out for all the pollutants. The results are illustrated in Fig. 12.

As evidenced in Fig. 12, the stability of the  $\text{MnO}_2\text{-SCS}$  sample was confirmed after three consecutive runs. Specifically, in each case, no significant differences were evidenced, thus demonstrating good deactivation resistance and effectiveness in the removal of pollutants.

Finally, to further verify the stability of  $\text{MnO}_2\text{-SCS}$ , time-on-stream (TOS) analyses were carried out under isothermal conditions, i.e. at the temperature at which the catalyst reaches 90 % of conversion, in order to investigate the stability at a nearly complete removal. TOS analyses were performed after the third runs for each pollutant tested and the results were displayed in Fig. 13.

As a whole, the catalyst showed interesting stability after 8 hours subjected to reaction conditions, at which the average conversion reached almost 90 % in dry and wet conditions. Precisely, the conversion of CO in dry (A) and wet (D) conditions remained constant for all the reaction time. In the case of ethylene (B), the conversion was kept constant for 3 h at the value of 93 %. After that, a slight decrease was recorded passing from 93 % to 88 %, resulting in a quite negligible loss of activity possibly due to the saturation of the active sites. Similar behavior was also evidenced in the case of propylene (C), showing a comparable loss of activity after 8 h (5 %). In the presence of moisture, the catalyst showed excellent stability in the case of CO oxidation (D), whereas for the VOCs (E, F), a less constant trend was observed compared to CO. The abatement performance was however still maintained after 8 h.

After the TOS analyses in dry and wet conditions, the spent catalyst

was analyzed by XRD to understand the behavior better and then compared with the fresh one. The results are reported in Figure S6. In all cases, no phase change was seen, as no peaks characteristic of other crystalline phases, i.e.,  $\text{Mn}_2\text{O}_3$  or  $\text{Mn}_3\text{O}_4$ , were detected. It was interesting to note the variation in the shape of the peaks in the regions between 25 and 40° and 50–60°. This variation could be due to the prolonged exposure to temperature and reagent mixture, which may have slightly modified the sample structure. However, the differences were not large and this was in line with the conversion profile in Fig. 13. To conclude, it was shown that the catalyst was able to operate for a prolonged time at the reaction conditions, maintaining its catalytic performance virtually unchanged, thus reflecting good structural stability and reproducibility over time.

### 3.3. The role of acidic properties and oxygen species on the reaction mechanism

The results of the characterizations previously mentioned are crucial for understanding why one catalyst was better than the others. However, the pollutants investigated present different features, thus they can interact in various manners, which could affect the reaction mechanism. To better understand which parameters and mechanisms differentiate the oxidation of CO from that of VOCs, other characterizations were carried out, in particular, to provide information on the acidity of the material. It is known that the acidity of the catalyst affects both the adsorption/desorption of a molecule, the strength of interaction between the catalyst and various gaseous reactive species [102] and the activation energy [103]. Based on these considerations,  $\text{NH}_3\text{-TPD}$  analysis was performed to evaluate the acidity of the samples. The detailed procedure is reported in the supporting information. The profiles obtained were reported in Fig. 14, whereas the amount of  $\text{NH}_3$  desorbed was included in Table 4.

Generally, the temperature of desorption of ammonia adsorbed on the Lewis acid sites is higher than that on Brønsted acid sites [104,105]. Considering the profiles obtained, the  $\text{NH}_3\text{-TPD}$  peaks could be classified as weak acidity at relatively low temperatures (100–250 °C), and medium/strong acidity at higher temperatures [106,107]. By considering the total amount of ammonia desorbed, the sample synthesized through the nanocasting procedure exhibited a slightly higher value compared to the other samples, as can be seen in Table 4, even if it is

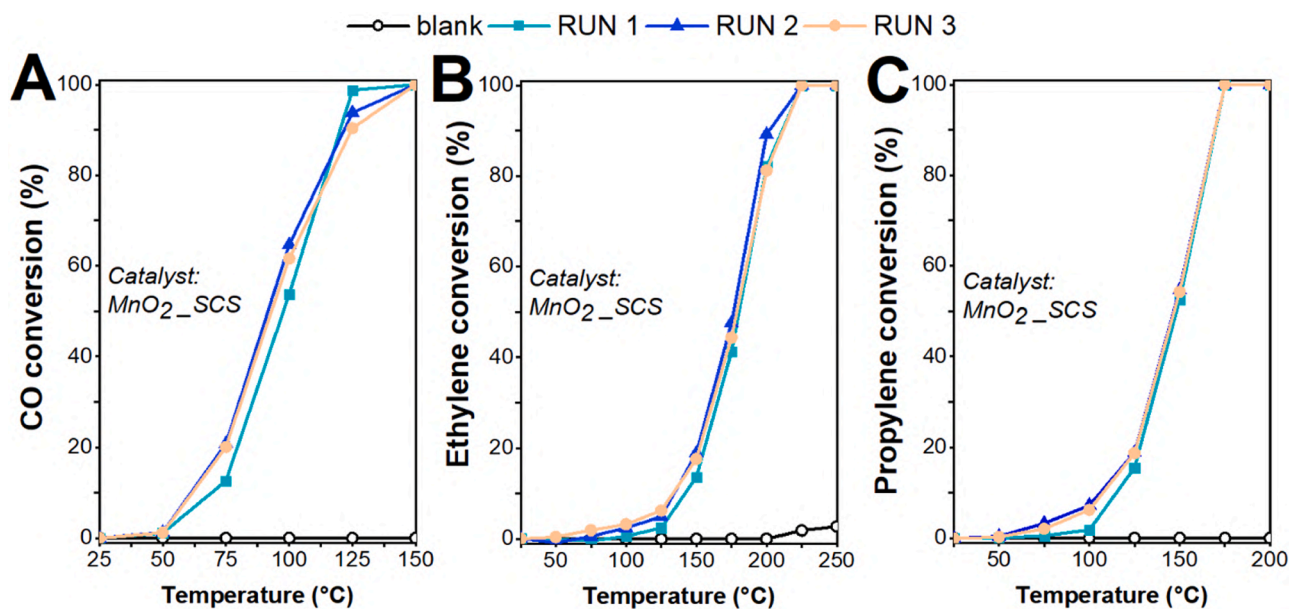


Fig. 12. Three consecutive runs of catalytic oxidation of 100 ppm of CO (A), ethylene (B), and propylene (C), 21 %vol.  $\text{O}_2$  and  $\text{N}_2$  to balance over 50 mg of  $\text{MnO}_2\text{-SCS}$ .

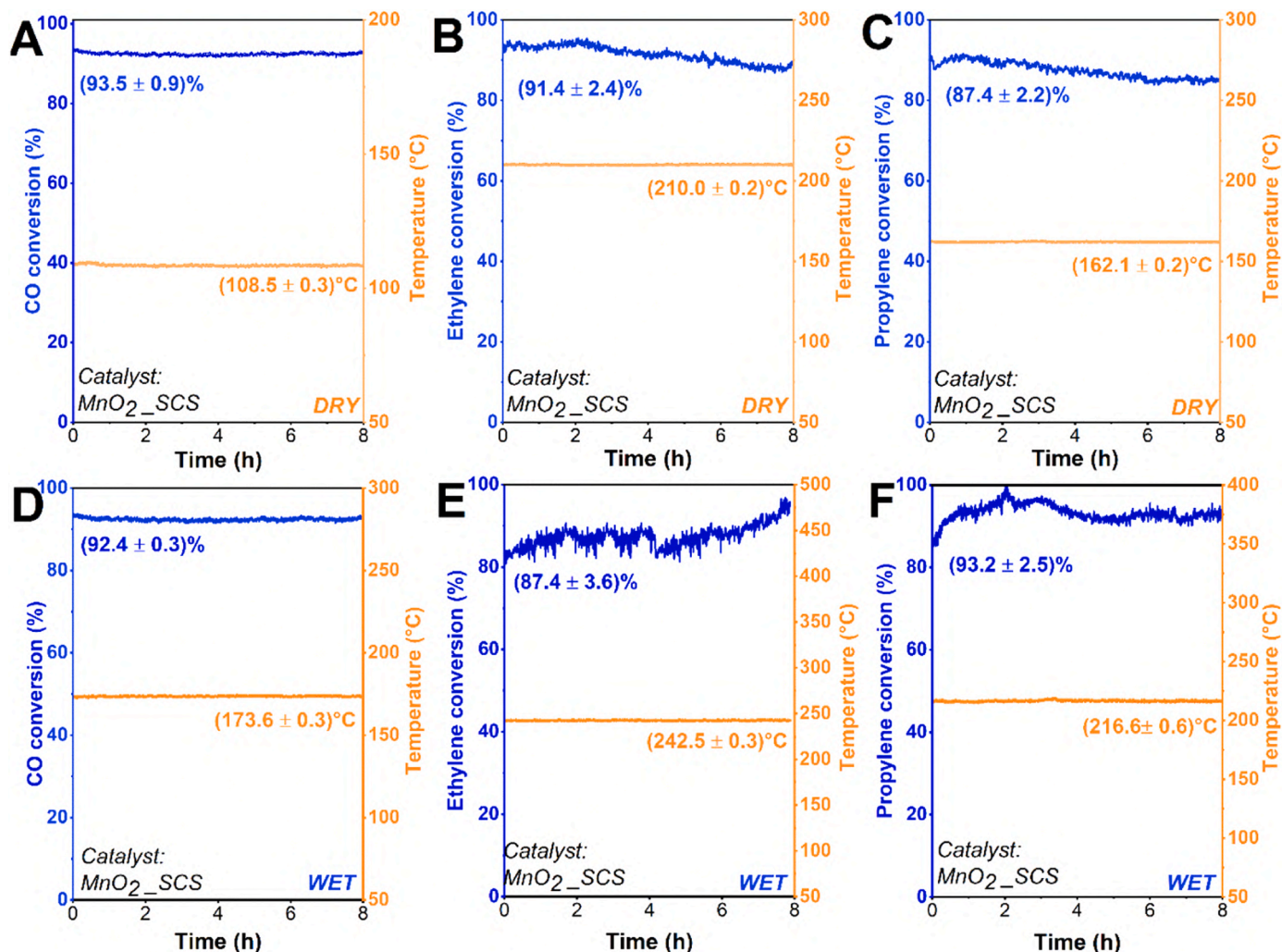


Fig. 13. Time-on-stream (TOS) analysis performed at isothermal condition T90, by feeding polluted air in dry and wet conditions with 100 ppm of CO (A, D), ethylene (B, E), and propylene (C, F), respectively, over 50 mg of catalyst.

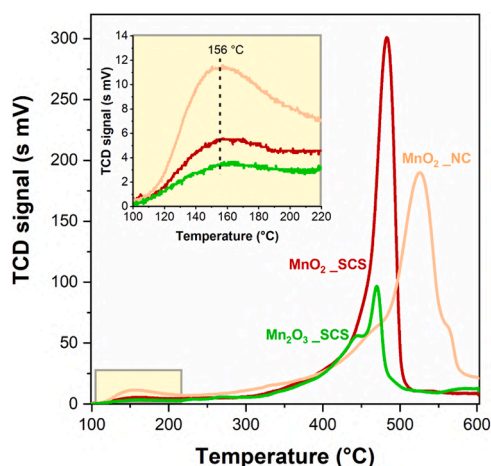


Fig. 14. NH<sub>3</sub>-TPD profiles of the synthesized materials.

very similar to that of MnO<sub>2</sub>\_SCS. This difference, however, should be only ascribed to the higher specific surface area of the MnO<sub>2</sub>\_NC sample. Indeed, when the values are normalized with respect to the SSA (mmol m<sup>-2</sup>), both the samples synthesized through the SCS procedure presented a higher amount of acidic sites compared to the NC sample. In

Table 4

Total NH<sub>3</sub>-desorption normalized per mass of catalyst (mmol g<sub>cat</sub><sup>-1</sup>) and per unit of surface area (mmol m<sup>-2</sup>) for all the synthesized manganese oxide samples.

Sample	Normalized NH <sub>3</sub> desorption mmol g <sub>cat</sub> <sup>-1</sup>	Normalized NH <sub>3</sub> desorption mmol m <sup>-2</sup>
MnO <sub>2</sub> _NC	3.429	0.034
MnO <sub>2</sub> _SCS	3.348	0.094
Mn <sub>2</sub> O <sub>3</sub> _SCS	1.280	0.064

particular, MnO<sub>2</sub>\_SCS exhibited the highest amount of NH<sub>3</sub> desorbed, which was almost twice as much as Mn<sub>2</sub>O<sub>3</sub>\_SCS and three times as much as MnO<sub>2</sub>\_NC.

Acidic sites play a pivotal role in the oxidation of different molecules, for example, ethylene [108]. Specifically, considering the results of the catalytic tests, and those of the physico-chemical characterizations, it was possible to hypothesize a different mechanism occurring in the CO, ethylene, and propylene oxidation. Indeed, considering the nature of the molecules under investigation, ethylene has a pK<sub>a</sub> of around 44, while the one of propylene is around 43. Although these values are very similar, propylene is slightly more acidic than ethylene due to the stabilization provided by the alkyl group. Therefore, ethylene, being more 'basic' than propylene, is more attracted to the acidic sites of the catalyst. This fact is also closely correlated with the activation energy, as revealed in the following paragraph. On the other hand, carbon

monoxide is almost neutral, so the presence of acid sites is secondary in this case. In fact, it can be assumed that VOCs follow a degradation mechanism on acid sites (an acid-base mechanism) that is different from that of CO, for which other properties are more impactful (e.g. redox properties) [109].

Besides the acidic properties, the presence of reactive oxygen species plays an important role in oxidation reactions as well. Generally, the oxidation of CO and VOCs is believed to occur through a Mars Van Krevelen-like (MvK) redox mechanism [52,109,110]. The main assumption is that the pollutant reacts with oxygen atoms in the catalyst rather than the oxygen in the gas phase. The role of gaseous O<sub>2</sub> is to reoxidize the catalyst, allowing a surface redox cycle. Therefore, the high reducibility of the catalyst is favorable for improving the activity because of the increased mobility of lattice oxygen. Considering the results obtained through H<sub>2</sub>-TPR and O<sub>2</sub>-TPD, MnO<sub>2</sub>\_SCS was recognized to have the highest redox properties compared to the other samples. Since this material was also the best-performing catalyst, temperature-programmed surface reaction (TPSR) tests were carried out in an oxygen-free atmosphere over this sample, in order to further investigate the oxidation mechanism and oxygen reactivity. The results of TPSR tests in the absence of oxygen were reported in Fig. 15.

In all the cases, the reactant (CO or VOC) interacted with the catalyst even in the absence of oxygen. Moreover, the CO<sub>2</sub> production started at the same temperature detected during the normal tests performed in the presence of O<sub>2</sub> (see Fig. 10). Different CO<sub>2</sub> profiles were obtained depending on the pollutant investigated, but always presenting different peaks at low, mild, and high temperatures. This phenomenon could be ascribed to the involvement of different oxygen species in pollutant oxidation. Firstly, CO/VOCs react with the surface active oxygen of transition metal oxides, leading to a partial reduction of metal oxide. Subsequently, when all these species are consumed, sub-surface lattice oxygens act to make the reaction go ahead, and, finally, at higher temperatures, bulk lattice oxygens become the last source to continue the reaction. Of course, the profiles obtained in the presence and in the absence of O<sub>2</sub> are different. In the former case, the oxygen in the gas feed

continuously re-oxidized the partially reduced surface of the catalyst and the conversion profile assumes the classic sigmoidal shape. In the latter case, the reaction proceeds as long as the catalyst is able to release oxygens; when lattice oxygen starts to lack, the oxidation slows down and the conversion starts to decrease. It was also interesting to note that in the case of CO oxidation, CO<sub>2</sub> is the only product and the two profiles have an opposite behavior. Whereas, in the case of ethylene and propylene, CO production was also detected. This could be due to the fact that, initially, the catalyst was able to provide sufficient oxygen atoms to lead to a complete oxidation of the pollutant. As these species are consumed, oxidation becomes partial and CO is formed as a by-product. In the end, all the oxygens are consumed and the reaction no longer proceeds. The direct involvement of lattice oxygen observed during these tests suggested that the reaction occurs via the MvK-like mechanism.

### 3.4. Kinetic study

Further investigations were carried out through a kinetic study. The values of the reaction rates measured during CO, ethylene, and propylene oxidation over the catalysts were reported in Table 5.

Comparing the conversion rates of the samples obtained with the same procedure, namely MnO<sub>2</sub>\_SCS, and Mn<sub>2</sub>O<sub>3</sub>\_SCS, it was clear that the presence of MnO<sub>2</sub> as a prevalent crystalline phase enhanced the catalytic oxidation of the pollutants compared to the Mn<sub>2</sub>O<sub>3</sub>. Whereas, by comparing two samples with the same crystalline phase, namely MnO<sub>2</sub>\_SCS, and MnO<sub>2</sub>\_NC, it appeared clear the promoting effect of the SCS method of synthesis, which is in agreement with the physico-chemical characterizations.

Finally, the apparent activation energy (named E<sub>a</sub> from now on) was evaluated to provide a more complete investigation of the catalytic performance of the synthesized samples. Catalytic oxidation of CO and VOCs was modeled with a pseudo-homogeneous first-order reaction, which is suitable for these kinds of diluted pollutants [111,112]. The results are reported in Fig. 16 and Table 6.

In each case, the apparent activation energy was evaluated in the region of kinetic control. As illustrated, all the catalysts exhibited different values of E<sub>a</sub> and in all cases, the determination coefficient R<sup>2</sup> showed a value close to the unity (see Table S8), indicating a good experimental data fitting with the model. As a whole, the results showed that activation energy strongly depends on the preparation route and the structure of the catalysts. Precisely, Mn<sub>2</sub>O<sub>3</sub>\_SCS evidenced values that agreed with other works [58,112,113]; however, its activation energy was generally higher compared to that of the other samples investigated. In particular, MnO<sub>2</sub>\_SCS showed extremely promising values, reaching almost 50 kJ mol<sup>-1</sup>, 32 kJ mol<sup>-1</sup>, and 45 kJ mol<sup>-1</sup> for CO, ethylene, and propylene oxidation, respectively. Hence, this sample seems able to provide an alternative route for the reaction with lower activation energy. Surprisingly, the activation energy calculated for CO oxidation over MnO<sub>2</sub>\_SCS was extremely close to that of a sample containing gold, and even lower compared to other catalysts reported in the literature (e.g., octahedral molecular sieve) [109,114,115]. These interesting results suggest that the MnO<sub>2</sub>\_SCS sample is able to simultaneously reduce the activation energy barrier and enhance the pollutant degradation efficiency and could therefore lay the foundation for the design of the aforementioned catalyst on a commercial scale.

Moreover, for both the VOCs investigated, MnO<sub>2</sub>\_NC and Mn<sub>2</sub>O<sub>3</sub>\_SCS presented extremely similar values of apparent activation energies. This is in agreement with the results of NH<sub>3</sub>-TPD. As previously mentioned, both ethylene and propylene exhibit an alkaline behavior, and therefore, interact with the acidic sites of the catalyst through the acid-base mechanism. Since ethylene is more alkaline compared to propylene, it is much more attracted by the acidic sites of the catalyst. On the contrary, carbon monoxide is almost neutral, so the presence of acidic sites is secondary in this case. This could explain the different values of the activation energies and why the sample Mn<sub>2</sub>O<sub>3</sub>\_SCS performed

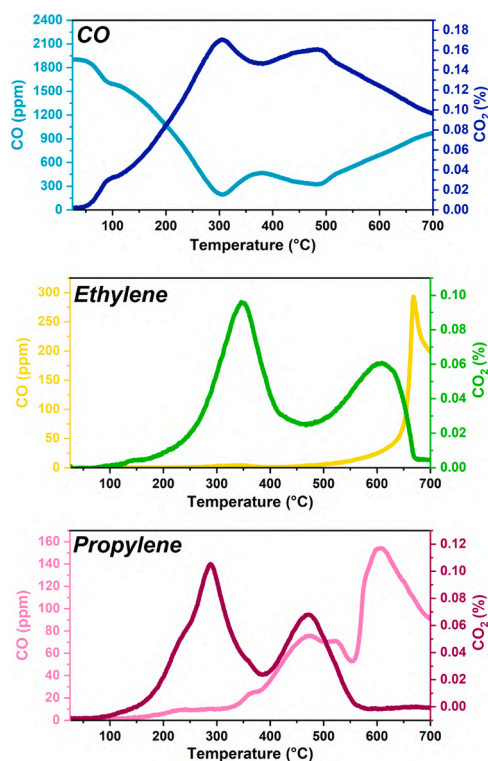


Fig. 15. TPSR profiles of MnO<sub>2</sub>\_SCS in the absence of oxygen for CO, ethylene, and propylene.

**Table 5**  
Conversion rates evaluated for CO, ethylene, and propylene oxidation over catalysts.

Sample	CO <sup>a</sup>		Ethylene <sup>b</sup>		Propylene <sup>b</sup>	
	[ $\mu\text{mol g}^{-1}\text{s}^{-1}$ ]	[ $\mu\text{mol m}^{-2}\text{s}^{-1}$ ]	[ $\mu\text{mol g}^{-1}\text{s}^{-1}$ ]	[ $\mu\text{mol m}^{-2}\text{s}^{-1}$ ]	[ $\mu\text{mol g}^{-1}\text{s}^{-1}$ ]	[ $\mu\text{mol m}^{-2}\text{s}^{-1}$ ]
MnO <sub>2</sub> _NC	1.419	0.014	0.339	0.003	0.828	0.008
MnO <sub>2</sub> _SCS	2.413	0.068	0.881	0.025	2.468	0.069
MnO <sub>2</sub> _comm	0.001	0.001	<0.001	<0.001	<0.001	<0.001
Mn <sub>2</sub> O <sub>3</sub> _SCS	0.088	0.004	0.163	0.005	0.801	0.035
Mn <sub>2</sub> O <sub>3</sub> _comm	0.006	0.004	0.007	0.005	0.001	0.001

<sup>a</sup> rate evaluated at 75 °C.

<sup>b</sup> rate evaluated at 125 °C.

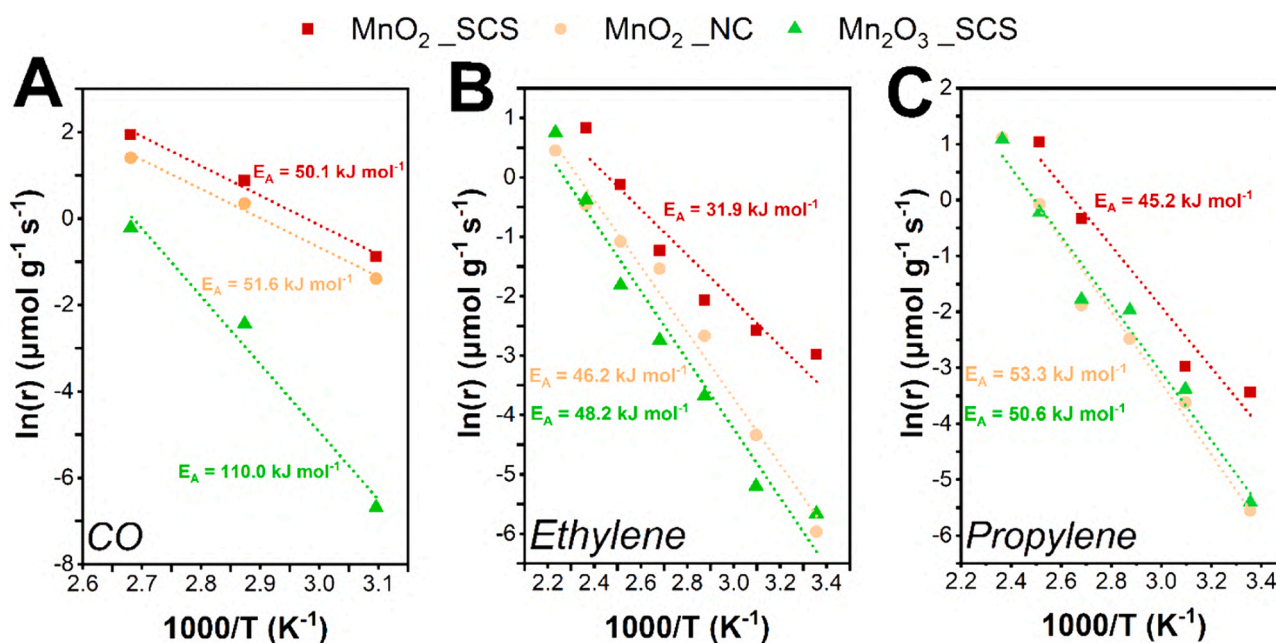


**Fig. 16.** Linear plot of the logarithm of the reaction rate ( $\mu\text{mol g}^{-1}\text{s}^{-1}$ ) versus  $1000/T$  ( $\text{K}^{-1}$ ) and the relative values of apparent activation energy ( $\text{kJ mol}^{-1}$ ) evaluated in the kinetic regime (conversion lower than 30 %), for CO (A), ethylene (B) and propylene (C) oxidation.

**Table 6**  
Comparison of conversion rates and the apparent activation energy evaluated for CO, ethylene, and propylene over MnO<sub>2</sub>\_SCS under dry and wet conditions.

Condition	Conversion rates [ $\mu\text{mol g}^{-1}\text{s}^{-1}$ ]			Activation energy $E_a$ [ $\text{kJ mol}^{-1}$ ]		
	CO (75 °C)	Ethylene (125 °C)	Propylene (125 °C)	CO	Ethylene	Propylene
dry	2.413	0.881	2.468	50.1	31.9	45.2
wet	0.037	0.049	0.159	79.4	36.2	67.7

comparably with the sample MnO<sub>2</sub>\_NC in the case of VOC oxidation. In fact, despite having worse chemical-physical properties than the other samples, the presence of high surface acidity helped the VOC oxidation. On the other hand, the CO molecule, as previously mentioned, is much more dependent on other chemical and physical properties, including  $O_w/O_b$ ,  $\text{Mn}^{4+}/\text{Mn}^{3+}$ , defects concentrations, etc. It is known that the presence of structural defects is responsible for the adsorption of oxygen on them [66]. Therefore, the higher the concentration of structural defects, the greater the adsorbed oxygen species responsible for CO oxidation and, consequently, the lower the activation energy. This is in agreement with what was observed for the three catalysts tested. In fact,  $O_w/O_b$  varies in the following order  $\text{MnO}_2\text{SCS} > \text{MnO}_2\text{NC} > \text{Mn}_2\text{O}_3\text{SCS}$  while  $E_{a\text{CO}}$  has an exactly opposite trend ( $\text{MnO}_2\text{SCS} < \text{MnO}_2\text{NC} < \text{Mn}_2\text{O}_3\text{SCS}$ ). This is also in agreement with the O<sub>2</sub>-TPD results. In fact, more energy during the reaction is required for the mobility of lattice oxygen for Mn<sub>2</sub>O<sub>3</sub>\_SCS [66].

Therefore, it is reasonable to assume that the number of surface defects for MnO<sub>2</sub>\_SCS and MnO<sub>2</sub>\_NC may be higher than that for Mn<sub>2</sub>O<sub>3</sub>\_SCS. This was also consistent with the preferential exposure of the reactive facet of MnO<sub>2</sub> samples and the difficulty of forming oxygen vacancy on Mn<sub>2</sub>O<sub>3</sub>, as detailed in the following section.

Table S9 reported the catalytic performance from the kinetic point of view of other existent materials in the literature. It is also crucial to point out that heating the catalysts leads to a reduction of the apparent  $E_a$  values. For this reason, the table reported the range at which the activation energy was evaluated. As a whole, the sample synthesized in this work, in particular MnO<sub>2</sub>\_SCS, exhibited promising values of T10, T50, T90, and activation energy. Some catalysts showed values of activation energy similar to those evaluated for MnO<sub>2</sub>\_SCS, but the range of temperature was wider, while the sample investigated in this work was active even at lower temperatures. In some cases, the catalytic performance was comparable with that obtained in this work, but a higher

catalyst mass was used in the test, or the synthesis technique adopted was more laborious and reagent-consuming with respect to the SCS technique.

Finally, a comparison of kinetic study under dry and wet conditions was proposed for the  $\text{MnO}_2\text{-SCS}$  sample. For all three pollutants tested, the reaction rates in the presence of moisture are lower, indicating slower kinetics due to the moisture hindering the pollutant from reaching the active sites. Accordingly, the activation energies are higher, as the presence of moisture increases the energy barrier of the reaction. However, although  $\text{MnO}_2\text{-SCS}$  exhibited higher activation energy under wet conditions than under dry conditions, the values were not far from those calculated under dry conditions for  $\text{MnO}_2\text{-NC}$  and  $\text{Mn}_2\text{O}_3\text{-SCS}$ .

### 3.5. Correlation between catalytic activity and physico-chemical properties

The catalytic performances are strictly correlated with the results of the physico-chemical characterizations, as can be seen in Fig. 17. Taking into account the results obtained from  $\text{N}_2$ -physisorption analysis, both commercial samples exhibited the worst results. Precisely, both of them presented very low specific surface area (see Table 1) which affected the number of active sites available to pollutants and increased intraparticle diffusion limitations, since they seemed to be non-porous, thus limiting the movement of the molecules. In fact, by performing some simulations for the CO molecule, it was found that the minimum pore diameter of the catalyst to avoid intraparticle diffusion limitation should be higher than 9 nm, as evaluated by preliminary calculation. As a result, by considering the conversion rates of  $\text{MnO}_2\text{-comm}$  and  $\text{Mn}_2\text{O}_3\text{-comm}$  toward all pollutants (see Table 5), no activity was detected at the temperature of 75 °C and 125 °C, for CO and both VOCs respectively, due to the inability of pollutants to reach all the active sites.

Concerning  $\text{MnO}_2\text{-NC}$ ,  $\text{MnO}_2\text{-SCS}$ , and  $\text{Mn}_2\text{O}_3\text{-SCS}$ , their catalytic performances can be explained by taking into account the results of  $\text{H}_2$ -TPR and  $\text{O}_2$ -TPD, crystallites dimension, and crystalline phases. Regarding temperature-programmed techniques, the catalytic performances were in close agreement with the reducibility of the samples, revealing the catalytic role of oxygen species [52]. In fact, it is well known that the presence of plentiful reactive lattice oxygen atoms can

greatly improve the catalytic oxidation of pollutants [33]. As demonstrated from  $\text{H}_2$ -TPR and  $\text{O}_2$ -TPD analyses, even if the range at which the first peak appears (both for  $\text{H}_2$  and  $\text{O}_2$ ) was ca. the same for all the synthesized catalysts, by comparing the amount of  $\text{H}_2$  consumed and  $\text{O}_2$  desorbed, related to the first peak (see Table S5 and Table S6),  $\text{MnO}_2\text{-SCS}$  sample showed the highest values in both cases, and this was correlated to higher oxygen mobility. Thus, it could be possible to associate the higher quantities of lattice oxygen species with the higher catalytic activity of  $\text{MnO}_2$  catalysts [46]. Furthermore, considering the synthesized samples, it can be seen that the crystal structure has an effect on the redox properties and mobility of the oxygens. If the crystal structures become more compact, as revealed from FESEM and AFM, the mobility of oxygen and the reducibility of the catalyst decreases. This affects the release and replenishment of lattice oxygen, which is crucial in the VOC oxidation reaction. Therefore, the reducibility of the catalyst is closely related to the catalytic activity. As reported in the literature, the reducibility of  $\text{MnO}_2$  is higher than that of  $\text{Mn}_2\text{O}_3$  [63] and this is related to the degree of redox cycling of manganese ions on the surface. In fact, a higher amount of  $\text{Mn}^{4+}/\text{Mn}^{3+}$  leads to the highest activity [32] and this fact shows a strong correlation with the average oxidation states evaluated by TPR and XPS. Of course, other properties should be taken into account to explain the different catalytic activity among the samples, namely the structure and the composition. It is well known that the size and morphology of particles are crucial factors in determining the catalytic activity of manganese oxide catalysts in structure-sensitive reactions, such as CO and VOC oxidation [46,48]. This is especially true in the case of CO, for which its oxidation is highly influenced by the crystal size of catalysts. In particular, catalytic performance improves by reducing the crystal size of catalyst, since small particle sizes provide sufficient accessible active sites for the reactants [46]. This could explain the better behavior of  $\text{MnO}_2\text{-SCS}$  (7 nm) and  $\text{MnO}_2\text{-NC}$  (4 nm) in the CO oxidation compared to  $\text{Mn}_2\text{O}_3\text{-SCS}$  (62 nm). On the other hand, VOC oxidation appeared to be unaffected by crystallite size or surface area. In fact, although  $\text{Mn}_2\text{O}_3\text{-SCS}$  and  $\text{MnO}_2\text{-NC}$  exhibited completely different values of the specific surface area and crystallite dimensions (see Table 1), both samples showed comparable conversion trends, as highlighted in Figs. 10B and 10C, for ethylene and propylene, respectively. Consequently, the oxidation of VOCs appears to be influenced by

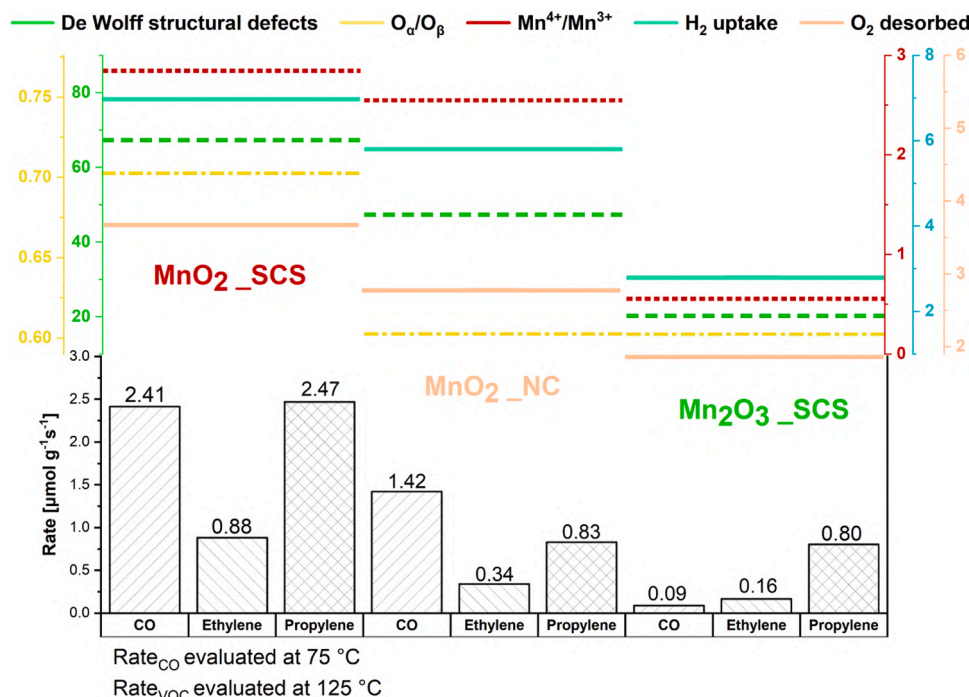


Fig. 17. Correlation between catalytic activity and the most significant physico-chemical properties for the synthesized manganese oxides.

additional parameters. Specifically, the lower performance observed for the  $\text{Mn}_2\text{O}_3\text{-SCS}$  sample, in comparison to the  $\text{MnO}_2\text{-SCS}$ , can be attributed to differences in terms of defects and overall morphology. AFM results reveal a slightly lower surface roughness for the former (0.96 nm) compared to the latter (1.14 nm), alongside a different surface-to-volume ratio (0.27 for  $\text{MnO}_2\text{-SCS}$  versus 0.12 for  $\text{Mn}_2\text{O}_3\text{-SCS}$ ). This fact further confirms that the structural and morphological properties significantly impact the catalytic performance. Moreover, studies have found that the phase structure as well as the oxidation state of manganese can significantly affect the catalytic activity of  $\text{MnO}_2$  (i.e., higher Mn average oxidation states mean higher reactivity) [34,48,63,116–119]. In fact, in the mechanism of MvK that occurs in VOC oxidation on  $\text{MnO}_2$ , firstly the lattice oxygen is desorbed, and many oxygen vacancies are created in the framework. Simultaneously, Mn decreases its oxidation state, and the desorbed oxygen can directly oxidize VOCs and CO [46,119]. Thus, having manganese oxide with a higher oxidation state could be beneficial for the removal of pollutants. Specifically, XPS revealed that the amount of  $\text{Mn}^{4+}$  was the highest in  $\text{MnO}_2\text{-SCS}$  compared to the other synthesized samples; in particular, it was 1.7 times higher than the amount in  $\text{Mn}_2\text{O}_3\text{-SCS}$  and 2.1 times higher than the value in  $\text{MnO}_2\text{-NC}$ . This could be another reason why the  $\text{MnO}_2\text{-SCS}$  sample exhibited superior activity compared to  $\text{Mn}_2\text{O}_3\text{-SCS}$  and  $\text{MnO}_2\text{-NC}$ , also in agreement with the outcomes of AOS evaluated from XPS. Another crucial parameter is the surface acidity of the catalysts, which is responsible for the acid-base mechanism in VOC oxidation. The differences between acid sites on the three catalysts may result from their specific structural features and exposed facets, leading to distinct catalytic performance. Considering the results of  $\text{NH}_3\text{-TPD}$ ,  $\text{Mn}_2\text{O}_3\text{-SCS}$  desorbed twice as much ammonia as the nanocasting sample per unit surface area. This may indicate a higher concentration of surface acid sites that favor the oxidation of VOCs. Finally, by comparing the performance of the same crystalline phase, namely  $\text{MnO}_2\text{-SCS}$  and  $\text{MnO}_2\text{-NC}$ , surprisingly it seemed that surface area was not the major reason for the different reactivity observed. Therefore, it could be considered a secondary parameter determining  $\text{MnO}_2$  reactivity, as reported in the literature [119]. Therefore, the superior performance of  $\text{MnO}_2\text{-SCS}$  compared to  $\text{MnO}_2\text{-NC}$  may be related to the different distribution of crystalline phases, mainly pyrolusite and ramsdellite, as demonstrated by XRD and Raman analyses. As previously mentioned, both catalysts presented a  $\gamma\text{-MnO}_2$  phase, which is reported to be more reactive than  $\alpha\text{-}$ ,  $\beta\text{-}$ , and  $\delta\text{-MnO}_2$  and other pure phases, due to the high amount of active surface oxygen species [116,119,120]. In fact,  $\gamma\text{-MnO}_2$  has both edge- and corner-sharing  $\text{MnO}_6$  deriving from the intergrowth tunnels of pyrolusite and ramsdellite and this is reflected in more accessible active sites [119]. Notably, not only the interaction between  $\beta\text{-}$  and  $\text{R-}$  phases enhanced the catalytic performance thanks to their synergy, but also their distribution in the structure was revealed as a crucial parameter since different percentage affects the amount of structural defects, mainly De Wolff defects. XRD results revealed that  $\text{MnO}_2\text{-SCS}$  had a pyrolusite to ramsdellite ratio of 5.5, while  $\text{MnO}_2\text{-NC}$  showed a ratio of 1.2. In fact, the results suggested that the presence of a higher percentage of pyrolusite, thus a higher amount of De Wolff defects, significantly increases the catalytic performance, leading to an increase in defects in the SCS sample, both in terms of mobility of oxygens and  $\text{Mn}^{4+}$  species. Moreover, surface defect sites demonstrate high oxidation activity because they are likely to generate active oxygen species, including surface oxygen species and highly reactive lattice oxygen species [63].

The TEM images provide crucial information about the exposed facets, which affect the physico-chemical properties and the catalytic activity. In fact, materials with the same composition ( $\text{MnO}_x$  in this case) but different structures or morphology may show diverse catalytic activity due to the preferential exposure of different active facets [4]. Theoretically, the reactivity and activity of facets depend on their surface energy: the higher the surface energy, the higher the reactivity in heterogeneous reactions [121]. By comparing  $\text{MnO}_2\text{-SCS}$  and  $\text{MnO}_2\text{-NC}$

samples, it was observed that both exposed the  $\text{MnO}_2$  (1 0 1) facet, which is one of the most reactive. In fact, from DFT calculations present in the literature [86], it was noticed that this facet exhibits the highest surface energy among all the  $\text{MnO}_2$  polymorphs, ca.  $2.4 \text{ J m}^{-2}$ . In addition, both samples also exhibited the presence of  $\text{MnO}_2$  (1 1 0) facet, which is both the most thermodynamically stable (since the surface energy is very low), the most redox-capable surface [122], and the most favorable for the generation of the oxygen vacancies [123]. This facet is also essential in understanding the acidity of the catalyst investigated in this work. In fact,  $\text{MnO}_2$ (1 1 0) presents no stable chemical adsorption for  $\text{NH}_3$ , except on the  $\text{Mn}^{4+}$  site on the surface. This fact indicates that this site is a highly stable chemisorption site for  $\text{NH}_3$  as well as a Lewis acid site [122]. Therefore, once again, the presence of a high  $\text{Mn}^{4+}/\text{Mn}^{3+}$  ratio, as highlighted by XPS, plays a pivotal role. This was also consistent with the highest reducibility of the  $\text{MnO}_2\text{-SCS}$  sample and its AOS evaluated from the profiles of  $\text{H}_2\text{-TPR}$ : the higher the oxidation state, the higher the activity of the sample. In addition, it is interesting to note that the different percentages of  $\beta\text{-}$  and  $\text{R-}$  phases within the structure, hence the different concentrations of De Wolff structural defects, cause the exposure of additional facets that may be responsible for catalytic activity. Among these, particular attention is devoted to the (2 1 0) facet, which, has a surface energy of  $1.8 \text{ J m}^{-2}$  [86]. In fact, this exposed facet played a pivotal role in tuning the catalytic performance, as reported in different works [124,125]. However, although both samples exhibited the same more reactive facets, they had different catalytic activities. Normalizing against the most intense peak obtained from the XRD analysis, it was observed that  $\text{MnO}_2\text{-SCS}$  had a higher percentage of  $\text{MnO}_2$ (2 1 0) than the  $\text{MnO}_2\text{-NC}$  sample (34 % in the former and 17 % in the latter), implying a higher activity. Furthermore, the SCS sample also exposed (1 1 1) crystal planes, that were not detected in the NC sample. This facet consists of high-density ( $1 \times 1$ ) tunnels [126], which are suitable to effectively prevent structural collapse, allowing high-rate performance and durable cyclability, as revealed in the following section. Finally, the presence of  $\text{Mn}_2\text{O}_3$  impurity structure could be beneficial. In fact, the  $\text{Mn}_2\text{O}_3$  (2 2 2) facets are more active for CO oxidation than the  $\text{MnO}_2$  (1 1 0) ones, which contributed to superior performance [46]. Furthermore,  $\text{Mn}_2\text{O}_3$  (2 2 2) facets can also favor the adsorption of  $\text{NH}_3$ . This means that this facet may be suitable for the adsorption of basic molecules [127], i.e., VOCs since they exhibit a basic behavior, as previously mentioned. Moreover, the presence of  $\text{Mn}_2\text{O}_3$  impurity favors the formation of more Mn defects [86], leading to the exposure of specific facets [121], and, in some cases,  $\text{MnO}_2\text{-Mn}_2\text{O}_3$  interfaces could facilitate the formation of oxygen vacancy [128], leading to extremely promising material for VOCs oxidation. However, although  $\text{Mn}_2\text{O}_3\text{-SCS}$  had reactive exposed facets, the oxygen vacancies are difficult to form on the  $\text{Mn}_2\text{O}_3$  (2 1 1) surface, due to the relatively higher formation energy, as revealed by Zhang et al. [123] from DFT calculations. This could be another reason concerning the poorest performance of  $\text{Mn}_2\text{O}_3\text{-SCS}$ . All these results suggested that the domains in the structures cooperated synergistically: the different crystalline phases, as well as the different concentrations of structural defects, led to the higher activity of the  $\text{MnO}_2\text{-SCS}$  sample thanks to the exposure of precise reactive facets which enhanced the acidity, the surface reducibility, and the generation of oxygen vacancies.

Comparing the results obtained with the existing literature (see Table S9), the catalysts analyzed in this work proved to be significantly high-performing, offering considerable advantages in terms of catalytic activity, efficiency, and cost. These materials exhibited significantly superior activity compared to other manganese oxides, which were also often obtained by more complex synthesis techniques. The presence of multiple crystalline phases plays a crucial role in improving their characteristics. In particular, these multiphase structures enhance the presence of defects, which not only contribute to improved catalytic activity but also serve as an important source for the generation of reactive oxygen species. This is a significant advantage over other materials, where complex synthesis can limit the abundance of defects and

reactive species. A particularly relevant aspect is the synthesis method used, i.e. SCS. This technique not only stands out for its high efficiency, but is also less complex than other methods. It is easy to replicate and allows optimization to obtain defective structures, which are crucial for improving catalytic performance. This makes our approach not only innovative but also practical and adaptable, facilitating the production and application of these materials.

#### 4. Conclusions

A set of mesoporous manganese oxides was prepared and tested for the total removal of pollutants (namely, CO, ethylene, and propylene). The effect of different crystalline phases ( $\text{MnO}_2$  and  $\text{Mn}_2\text{O}_3$ ) was investigated by synthesizing two samples ( $\text{MnO}_2\text{-SCS}$  and  $\text{Mn}_2\text{O}_3\text{-SCS}$ ) through the same procedure (SCS). Subsequently, the most performing phase was further prepared with another method ( $\text{MnO}_2\text{-NC}$ ), to explore how the different distribution of polymorphs affects the structural defects and the catalytic activity of this material. The results revealed that, in all cases, the most promising catalyst was  $\text{MnO}_2\text{-SCS}$ . The enhanced performance can be attributed to the higher mobile oxygens that improve the sample's activity compared to the other catalysts tested, the highest surface acidity that is crucial for the VOCs oxidation, but also thanks to uncommon morphology and the synergy between different crystalline phases which increase the structural defect exposing specific reactive facets, and enhance the accessibility of active sites. The morphology may enhance catalytic performance, probably due to the formation of more surface  $\text{Mn}^{4+}$  and active oxygen species in the case of the SCS sample. Furthermore, the presence of simultaneous crystalline phases is responsible for the discontinuity of the structure, and this fact generates structural defects, creating a very reactive material. Interestingly, although a high surface area often leads to a higher number of active sites and thus a higher catalytic activity, the results showed that this parameter is not decisive. As expected, in the presence of moisture, there was competitive adsorption between moisture and VOCs, which is common at low temperatures, but the results revealed that  $\text{MnO}_2\text{-SCS}$  showed promising performances, even though the removal temperatures were slightly higher than under dry conditions. Moreover, the sample revealed outstanding stability after three consecutive catalytic runs and long-term stability under isothermal conditions at T90 after 8 hours in all cases. Finally, kinetic studies highlighted that  $\text{MnO}_2\text{-SCS}$  provides an alternative catalytic pathway with the lowest apparent activation energy, reaching 50, 32, and 45  $\text{kJ mol}^{-1}$  for CO, ethylene, and propylene oxidation, respectively. According to the high catalytic performance, kinetic study, and stability tests,  $\text{MnO}_2\text{-SCS}$  may potentially be used as a promising catalyst for environmental applications, in particular, to remove indoor pollutants that are more difficult to oxidate at low/mild temperatures. Based on the results achieved, this catalyst could be employed in a device placed in a ventilation system, such as a hood in a kitchen that sucks in hot fumes, or in a purification section operating at mild temperatures ( $> 100^\circ\text{C}$ ) to treat the air taken from the contaminated environment (office, canteen, kitchen, warehouse, etc.). Compared with expensive noble metals, transition metal oxide catalysts, like  $\text{MnO}_2$ , are much cheaper and could be valid alternatives to deal with the removal of pollutants. To conclude, the relatively novel SCS method can be considered highly promising, cost-effective, and efficient for the bulk production of nano and mesostructured materials with enhanced redox properties and high structural defects. However, the NC procedure can be considered a valid alternative to other methods, to obtain materials with good redox properties and high surface area, suitable as supports for the deposition of other types of nanoparticles.

#### Funding

This study was carried out within the MICS (Made in Italy – Circular and Sustainable) Extended Partnership and received funding from the European Union Next-GenerationEU (PIANO NAZIONALE DI RIPRESA E

RESILIENZA (PNRR) – MISSIONE 4 COMPONENTE 2, INVESTIMENTO 1.3 – D.D. 1551.11–10–2022, PE00000004) and the PON Ricerca e Innovazione “REACT-EU” project (DM 1062/21). This manuscript reflects only the authors' views and opinions, neither the European Union nor the European Commission can be considered responsible for them.

#### Credit authorship contribution statement

**Nadia Grifasi:** Data curation, Formal analysis, Investigation, Writing - original draft, reviewed draft. **Enrico Sartoretti:** Data curation, Formal analysis, Investigation, Writing - original draft, reviewed draft. **Daniel Montesi:** Data curation, Formal analysis, Investigation. **Samir Bensaid:** Investigation, Writing. **Nunzio Russo:** Investigation, Writing. **Fabio Deorsola:** Investigation, Writing, Funding. **Debora Fino:** Investigation, Writing, Funding. **Chiara Novara:** Investigation, Writing, **Fabrizio Giorgis:** Investigation, Writing, **Marco Piumetti:** Investigation, Writing, Supervision.

#### Declaration of Competing Interest

The authors declare that they have no known competing financial interests or personal relationships that could have appeared to influence the work reported in this paper

#### Acknowledgment

The authors thank Camilla Galletti, Salvatore Guastella, Marco Allione, and Maria Carmen Valsania for performing XRD, XPS, and HR-TEM analyses. The authors also acknowledge the funding received by Ministero dell'Università e della Ricerca under the Dipartimento di Eccellenza 2018-2022 program.

#### Appendix A. Supporting information

Supplementary data associated with this article can be found in the online version at [doi:10.1016/j.apcatb.2024.124696](https://doi.org/10.1016/j.apcatb.2024.124696).

#### Data Availability

Data will be made available on request.

#### References

- [1] Y. Guo, M. Wen, G. Li, T. An, Recent advances in VOC elimination by catalytic oxidation technology onto various nanoparticles catalysts: a critical review, *Appl. Catal. B* 281 (2021), <https://doi.org/10.1016/j.apcatb.2020.119447>.
- [2] United States Environmental Protection Agency, Volatile Organic Compounds' Impact on Indoor Air Quality | US EPA, United States Government, 2022. ([https://www.epa.gov/indoor-air-quality-iaq/volatile-organic-compounds-impact-indoor-air-quality](https://www.epa.gov/indoor-air-quality-iaq/volatile-organic-compounds-impact-indoor-air-quality#Health_Effects%0Ahttps://www.epa.gov/indoor-air-quality-iaq/volatile-organic-compounds-impact-indoor-air-quality)).
- [3] U.S. Environmental Protection Agency, An Introduction to Indoor Air Quality: Volatile Organic Compounds (VOCs), U.S. EPA, 2011. (<http://www.epa.gov/iaq/voc.html>).
- [4] H. Huang, Y. Xu, Q. Feng, D.Y.C. Leung, Low temperature catalytic oxidation of volatile organic compounds: a review, *Catal. Sci. Technol.* 5 (2015) 2649–2669, <https://doi.org/10.1039/c4cy01733a>.
- [5] H. Chen, R. Zhang, H. Wang, W. Bao, Y. Wei, Encapsulating uniform Pd nanoparticles in TS-1 zeolite as efficient catalyst for catalytic abatement of indoor formaldehyde at room temperature, *Appl. Catal. B* 278 (2020), <https://doi.org/10.1016/j.apcatb.2020.119311>.
- [6] D. Zhu, Y. Huang, J. Ji Cao, S.C. Lee, M. Chen, Z. Shen, Cobalt nanoparticles encapsulated in porous nitrogen-doped carbon: oxygen activation and efficient catalytic removal of formaldehyde at room temperature, *Appl. Catal. B* 258 (2019), <https://doi.org/10.1016/j.apcatb.2019.117981>.
- [7] Z. Di, H. Chen, R. Zhang, H. Wang, J. Jia, Y. Wei, Significant promotion of reducing treatment on Pd/TS-1 zeolite for formaldehyde catalytic purification at ambient temperature, *Appl. Catal. B* 304 (2022), <https://doi.org/10.1016/j.apcatb.2021.120843>.
- [8] J. Ye, B. Cheng, J. Yu, W. Ho, S. Wageh, A.A. Al-Ghamdi, Hierarchical Co3O4-NiO hollow dodecahedron-supported Pt for room-temperature catalytic formaldehyde decomposition, *Chem. Eng. J.* 430 (2022), <https://doi.org/10.1016/j.cej.2021.132715>.

- [9] K. Vellingiri, K. Vikrant, V. Kumar, K.-H. Kim, Advances in thermocatalytic and photocatalytic techniques for the room/low temperature oxidative removal of formaldehyde in air, *Chem. Eng. J.* 399 (2020) 125759, <https://doi.org/10.1016/j.cej.2020.125759>.
- [10] Z. Wang, J. Pei, J. Zhang, Catalytic oxidization of indoor formaldehyde at room temperature - Effect of operation conditions, *Build. Environ.* 65 (2013) 49–57, <https://doi.org/10.1016/j.buildenv.2013.03.007>.
- [11] Y. Qi, C. Li, H. Li, H. Yang, J. Guan, Elimination or removal of ethylene for fruit and vegetable storage via low-temperature catalytic oxidation, *J. Agric. Food Chem.* 69 (2021) 10419–10439.
- [12] D.A. Morgott, Anthropogenic and biogenic sources of Ethylene and the potential for human exposure: A literature review, *Chem. Biol. Inter.* 241 (2015) 10–22, <https://doi.org/10.1016/j.cbi.2015.08.012>.
- [13] D.A. Morgott, The human exposure potential from propylene releases to the environment, *Int J. Environ. Res Public Health* 15 (2018), <https://doi.org/10.3390/ijerph15010066>.
- [14] S. Jin, L. Zhong, X. Zhang, X. Li, B. Li, X. Fang, Indoor volatile organic compounds: concentration characteristics and health risk analysis on a university campus, *Int J. Environ. Res Public Health* 20 (2023) 5829.
- [15] J. Senthilnathan, K.-H. Kim, J.-C. Kim, J.-H. Lee, H.N. Song, Indoor air pollution, sorbent selection, and analytical techniques for volatile organic compounds, *Asian J. Atmos. Environ.* 12 (2018) 289–310.
- [16] A. Vanker, P.M. Nduru, W. Barnett, F.S. Dube, P.D. Sly, R.P. Gie, M.P. Nicol, H. J. Zar, Indoor air pollution and tobacco smoke exposure: impact on nasopharyngeal bacterial carriage in mothers and infants in an African birth cohort study, *ERJ Open Res* 5 (2019).
- [17] B. You, W. Zhou, J. Li, Z. Li, Y. Sun, A review of indoor gaseous organic compounds and human chemical exposure: insights from real-time measurements, *Environ. Int* 170 (2022) 107611.
- [18] J.-Y. Chin, C. Godwin, E. Parker, T. Robins, T. Lewis, P. Harbin, S. Batterman, Levels and sources of volatile organic compounds in homes of children with asthma, *Indoor Air* 24 (2014) 403–415, <https://doi.org/10.1111/ina.12086>.
- [19] R. Zhao, H. Wang, D. Zhao, R. Liu, S. Liu, J. Fu, Y. Zhang, H. Ding, Review on catalytic oxidation of VOCs at Ambient Temperature, *Int J. Mol. Sci.* 23 (2022), <https://doi.org/10.3390/ijms232213739>.
- [20] I. Gee, Volatile Organic Compounds, *Indoor Built Environ.* 5 (1996) 187–188, <https://doi.org/10.1177/1420326X9600500311>.
- [21] WHO, An Introduction for Health Professionals, (2007) 1–33. ([https://www.epa.gov/sites/default/files/2015-01/documents/indoor\\_air\\_pollution.pdf](https://www.epa.gov/sites/default/files/2015-01/documents/indoor_air_pollution.pdf)).
- [22] Q. Zhao, Y. Zheng, C. Song, Q. Liu, N. Ji, D. Ma, X. Lu, Novel monolithic catalysts derived from in-situ decoration of Co3O4 and hierarchical Co3O4/MnOx on Ni foam for VOC oxidation, *Appl. Catal. B* 265 (2020), <https://doi.org/10.1016/j.apcatb.2019.118552>.
- [23] B. Faure, P. Alphonse, Co-Mn-oxide spinel catalysts for CO and propane oxidation at mild temperature, *Appl. Catal. B* 180 (2015) 715–725, <https://doi.org/10.1016/j.apcatb.2015.07.019>.
- [24] W. Tang, X. Wu, S. Li, X. Shan, G. Liu, Y. Chen, Co-nanocasting synthesis of mesoporous Cu-Mn composite oxides and their promoted catalytic activities for gaseous benzene removal, *Appl. Catal. B* 162 (2015) 110–121, <https://doi.org/10.1016/j.apcatb.2014.06.030>.
- [25] M. Piumetti, D. Fino, N. Russo, Mesoporous manganese oxides prepared by solution combustion synthesis as catalysts for the total oxidation of VOCs, *Appl. Catal. B* 163 (2015) 277–287, <https://doi.org/10.1016/j.apcatb.2014.08.012>.
- [26] M.J. Marin Figueredo, M. Piumetti, S. Bensaid, D. Fino, R. Nunzio, Catalytic oxidation of volatile organic compounds over porous manganese oxides prepared via sol-gel method, *Nanostruct. Catal. Environ. Appl.* (2021) 59–78, [https://doi.org/10.1007/978-3-030-58934-9\\_2](https://doi.org/10.1007/978-3-030-58934-9_2).
- [27] M. Dosa, M.J. Marin-figueredo, E. Sartoretto, C. Novara, F. Giorgis, S. Bensaid, D. Fino, N. Russo, M. Piumetti, Cerium-copper oxides synthesized in a multi-inlet vortex reactor as effective nanocatalysts for CO and ethene oxidation reactions, *Catalysts* 12 (2022), <https://doi.org/10.3390/catal12040364>.
- [28] M.V. Grabchenko, N.N. Mikheeva, G.V. Mamontov, M.A. Salaev, L.F. Liotta, O. V. Vodyankina, Ag/CeO2 composites for catalytic abatement of CO, Soot and VOCs, *Catalysts* 8 (2018), <https://doi.org/10.3390/catal8070285>.
- [29] M.J. Marin Figueredo, T. Andana, S. Bensaid, M. Dosa, D. Fino, N. Russo, M. Piumetti, Cerium-copper-manganese oxides synthesized via solution combustion synthesis (SCS) for Total Oxidation of VOCs, *Catal. Lett.* 150 (2020) 1821–1840, <https://doi.org/10.1007/s10562-019-03094-x>.
- [30] S. Royer, H. Duprez, Catalytic oxidation of carbon monoxide over transition metal oxides, *ChemCatChem* 3 (2011) 24–65, <https://doi.org/10.1002/cctc.201000378>.
- [31] M. Giuliano, M.C. Valsania, P. Ticali, E. Sartoretto, S. Morandi, S. Bensaid, G. Ricchiardi, M. Sgroi, Characterization of the evolution of noble metal particles in a commercial three-way catalyst: correlation between real and simulated ageing, *Catalysts* 11 (2021), <https://doi.org/10.3390/catal11020247>.
- [32] H. Zhou, W. Su, Y. Xing, J. Wang, W. Zhang, H. Jia, T. Yue, Progress of catalytic oxidation of VOCs by manganese-based catalysts, *Fuel* 366 (2024) 131305.
- [33] F. Kong, H. Zhang, H. Chai, B. Liu, Y. Cao, Insight into the crystal structures and surface property of manganese oxide on CO catalytic oxidation performance, *Inorg. Chem.* 60 (2021) 5812–5820, <https://doi.org/10.1021/acs.inorgchem.1c00144>.
- [34] K. Li, C. Chen, H. Zhang, X. Hu, T. Sun, J. Jia, Effects of phase structure of MnO2 and morphology of  $\delta$ -MnO2 on toluene catalytic oxidation, *Appl. Surf. Sci.* 496 (2019), <https://doi.org/10.1016/j.apsusc.2019.143662>.
- [35] J.H. Park, D.C. Kang, S.J. Park, C.H. Shin, CO oxidation over MnO2 catalysts prepared by a simple redox method: Influence of the Mn (II) precursors, *J. Ind. Eng. Chem.* 25 (2015) 250–257, <https://doi.org/10.1016/j.jiec.2014.11.001>.
- [36] C.S. Ha, S.S. Park, General synthesis and physico-chemical properties of mesoporous materials, 2019. ([https://doi.org/10.1007/978-981-13-2959-3\\_2](https://doi.org/10.1007/978-981-13-2959-3_2)).
- [37] X. Deng, K. Chen, H. Tüysüz, Protocol for the nanocasting method: preparation of ordered mesoporous metal oxides, *Chem. Mater.* 29 (2017) 40–52, <https://doi.org/10.1021/acs.chemmater.6b02645>.
- [38] F. Kleitz, S.H. Choi, R. Ryoo, Cubic Ia3d large mesoporous silica: synthesis and replication to platinum nanowires, carbon nanorods and carbon nanotubes, *Chem. Commun.* 3 (2003) 2136–2137, <https://doi.org/10.1039/b306504a>.
- [39] Y. Ren, Z. Ma, S. Dai, Nanosize control on porous  $\beta$ -MnO2 and their catalytic activity in CO oxidation and N2O decomposition, *Materials* 7 (2014) 3547–3556, <https://doi.org/10.3390/ma7053547>.
- [40] F. Jiao, A. Harrison, A.H. Hill, P.G. Bruce, Mesoporous Mn2O3 and Mn3O4 with crystalline walls, *Adv. Mater.* 19 (2007) 4063–4066, <https://doi.org/10.1002/adma.200700336>.
- [41] B.M.P. Kumar, K.H. Shivaprasad, R.S. Raveendra, R.H. Krishna, S. Karikkat, B. M. Nagabhushana, Preparation of MnO 2 nanoparticles for the adsorption of environmentally hazardous malachite green dye, *Int. J. Appl. Or. Innov. Eng. Manag.* 3 (2014) 102–106.
- [42] M.M. Moqaddam, M. Mirjalili, J.V. Khaki, S.M. Beidokhti, A new approach in the one-step synthesis of  $\alpha$ -MnO2 via a modified solution combustion procedure, *Nanoscale Adv.* 4 (2022) 3909–3918, <https://doi.org/10.1039/d2na00257d>.
- [43] B.D. Cullity, UoNotreDame, Elements of diffraction quasi-optics, 1994.
- [44] Z.A. Allothman, A review: fundamental aspects of silicate mesoporous materials, *Materials* 5 (2012) 2874–2902, <https://doi.org/10.3390/ma5122874>.
- [45] T. Franken, C. Mbaya Mani, R. Palkovits, Crystalline ordered mesoporous Cu0.25Co2.75O4 prepared with selected mesoporous silica templates and their performances as DeN2O catalysts, *Microporous Mesoporous Mater.* 221 (2016) 91–100, <https://doi.org/10.1016/j.micromeso.2015.09.019>.
- [46] S. Dey, V.V. Praveen Kumar, The performance of highly active manganese oxide catalysts for ambient conditions carbon monoxide oxidation, *Curr. Res. Green. Sustain. Chem.* 3 (2020) 100012, <https://doi.org/10.1016/j.crgsc.2020.100012>.
- [47] S.K. Ghosh, Diversity in the family of manganese oxides at the nanoscale: from fundamentals to applications, *ACS Omega* 5 (2020) 25493–25504, <https://doi.org/10.1021/acsomega.0c03455>.
- [48] H. Song, L. Xu, M. Chen, Y. Cui, C.E. Wu, J. Qiu, L. Xu, G. Cheng, X. Hu, Recent progresses in the synthesis of MnO2 nanowire and its application in environmental catalysis, *RSC Adv.* 11 (2021) 35494–35513, <https://doi.org/10.1039/d1ra06497e>.
- [49] S. Bernardini, F. Bellatreccia, G. Della Ventura, A. Sodo, A reliable method for determining the oxidation state of manganese at the microscale in Mn Oxides via Raman Spectroscopy, *Geostand. Geoanal. Res* 45 (2021) 223–244, <https://doi.org/10.1111/ggr.12361>.
- [50] A.M. Bystrom, The crystal structure of ramsdellite, an orthorhombic modification of MnO2, *Acta Chem. Scand.* 3 (1949) 163–173.
- [51] T.P. Moore, Ilfeld Harz Mountains: Thuringia, Germany, *Mineral. Rec.* 41 (2010) 481–506.
- [52] V.P. Santos, M.F.R. Pereira, J.J.M. Ôrfão, J.L. Figueiredo, The role of lattice oxygen on the activity of manganese oxides towards the oxidation of volatile organic compounds, *Appl. Catal. B* 99 (2010) 353–363, <https://doi.org/10.1016/j.apcatb.2010.07.007>.
- [53] H. Radinger, P. Connor, R. Stark, W. Jaegermann, B. Kaiser, Manganese oxide as an inorganic catalyst for the oxygen evolution reaction studied by X-Ray Photoelectron and Operando Raman Spectroscopy, *ChemCatChem* 13 (2021) 1175–1185, <https://doi.org/10.1002/cctc.202001756>.
- [54] N. Jabeen, Q. Xia, S.V. Savilov, S.M. Aldoshin, Y. Yu, H. Xia, Enhanced pseudocapacitive performance of  $\alpha$ -MnO2 by cation preinsertion, *ACS Appl. Mater. Interfaces* 8 (2016) 33732–33740.
- [55] M.A. Stranick, M.A. Stranick, MnO2 by XPS MnO 2 by XPS, *Surf. Sci. Spectra* 6 (2015) 31.
- [56] H.W. Nesbitt, D. Banerjee, Interpretation of XPS Mn(2p) spectra of Mn oxyhydroxides and constraints on the mechanism of MnO2 precipitation, *Am. Mineral.* 83 (1998) 305–315, <https://doi.org/10.2138/am-1998-3-414>.
- [57] Y. Wei, S. Jin, R. Zhang, W. Li, J. Wang, S. Yang, H. Wang, M. Yang, Y. Liu, W. Qiao, L. Ling, M. Jin, Preparation of mesoporous Mn-Ce-Ti-O aerogels by a one-pot sol-gel method for selective catalytic reduction of NO with NH3, *Materials* 13 (2020), <https://doi.org/10.3390/ma13020475>.
- [58] C. Feng, F. Jiang, G. Xiong, C. Chen, Z. Wang, Y. Pan, Z. Fei, Y. Lu, X. Li, R. Zhang, Y. Liu, Revelation of Mn4+–Osur-Mn3+ active site and combined Langmuir-Hinshelwood mechanism in propane total oxidation at low temperature over MnO2, *Chem. Eng. J.* 451 (2023), <https://doi.org/10.1016/j.cej.2022.138868>.
- [59] S.C. Kim, W.G. Shim, Catalytic combustion of VOCs over a series of manganese oxide catalysts, *Appl. Catal. B* 98 (2010) 180–185, <https://doi.org/10.1016/j.apcatb.2010.05.027>.
- [60] Y. Yang, P. Zhang, K. Hu, X. Duan, Y. Ren, H. Sun, S. Wang, Sustainable redox processes induced by peroxymonosulfate and metal doping on amorphous manganese dioxide for nonradical degradation of water contaminants, *Appl. Catal. B* 286 (2021) 119903, <https://doi.org/10.1016/j.apcatb.2021.119903>.
- [61] N.D. Wasalathanthri, T.M. SantaMaria, D.A. Kriz, S.L. Dissanayake, C.H. Kuo, S. Biswas, S.L. Suib, Mesoporous manganese oxides for NO2 assisted catalytic soot oxidation, *Appl. Catal. B* 201 (2017) 543–551, <https://doi.org/10.1016/j.apcatb.2016.08.052>.
- [62] Y. Liu, H. Zhou, R. Cao, X. Liu, P. Zhang, J. Zhan, L. Liu, Facile and green synthetic strategy of birnessite-type MnO2 with high efficiency for airborne

- benzene removal at low temperatures, *Appl. Catal. B* 245 (2019) 569–582, <https://doi.org/10.1016/j.apcatb.2019.01.023>.
- [63] J. Wang, H. Zhao, J. Song, T. Zhu, W. Xu, Structure-activity relationship of manganese oxide catalysts for the catalytic oxidation of (Chloro)-VOCs, *Catalysts* 9 (2019), <https://doi.org/10.3390/catal9090726>.
- [64] Y. Du, Q. Meng, J. Wang, J. Yan, H. Fan, Y. Liu, H. Dai, Three-dimensional mesoporous manganese oxides and cobalt oxides: High-efficiency catalysts for the removal of toluene and carbon monoxide, *Microporous Mesoporous Mater.* 162 (2012) 199–206, <https://doi.org/10.1016/j.micromeso.2012.06.030>.
- [65] Y. Dong, C. Su, K. Liu, H. Wang, Z. Zheng, W. Zhao, S. Lu, The catalytic oxidation of formaldehyde by FeOx-MnO<sub>2</sub>-CeO<sub>2</sub> catalyst: effect of iron modification, *Catalysts* 11 (2021), <https://doi.org/10.3390/catal11050555>.
- [66] K. Ramesh, L. Chen, F. Chen, Y. Liu, Z. Wang, Y.F. Han, Re-investigating the CO oxidation mechanism over unsupported MnO, Mn<sub>2</sub>O<sub>3</sub> and MnO<sub>2</sub> catalysts, *Catal. Today* 131 (2008) 477–482, <https://doi.org/10.1016/j.cattod.2007.10.061>.
- [67] M.J.M. Figueredo, C. Cocuzza, S. Bensaid, D. Fino, M. Piumetti, N. Russo, Catalytic abatement of volatile organic compounds and soot over manganese oxide catalysts, *Materials* 14 (2021), <https://doi.org/10.3390/ma14164534>.
- [68] M. Piumetti, S. Bensaid, T. Andana, M. Dosa, C. Novara, F. Giorgis, N. Russo, D. Fino, Nanostructured ceria-based materials: effect of the hydrothermal synthesis conditions on the structural properties and catalytic activity, *Catalysts* 7 (2017), <https://doi.org/10.3390/catal7060174>.
- [69] R. Phillips, K. Jolley, Y. Zhou, R. Smith, Influence of temperature and point defects on the X-ray diffraction pattern of graphite, *Carbon Trends* 5 (2021) 100124, <https://doi.org/10.1016/j.cartre.2021.100124>.
- [70] W.M. Dose, S.W. Donne, Thermal expansion of manganese dioxide using high-temperature in situ X-ray diffraction, *J. Appl. Crystallogr.* 46 (2013) 1283–1288, <https://doi.org/10.1107/S0021889813017846>.
- [71] T. Hatakeyama, N.L. Okamoto, T. Ichitsubo, Thermal stability of MnO<sub>2</sub> polymorphs, *J. Solid State Chem.* 305 (2022), <https://doi.org/10.1016/j.jssc.2021.122683>.
- [72] E. Corrao, F. Salomone, E. Giglio, M. Castellino, S.M. Ronchetti, M. Armandi, R. Pirone, S. Bensaid, CO<sub>2</sub> conversion into hydrocarbons via modified Fischer-Tropsch synthesis by using bulk iron catalysts combined with zeolites, *Chem. Eng. Res. Des.* 197 (2023) 449–465, <https://doi.org/10.1016/j.cherd.2023.07.052>.
- [73] C. Lin, S.A. Al-Muhtaseb, J.A. Ritter, Thermal treatment of sol-gel derived nickel oxide xerogels, *J. Solgel Sci. Technol.* 28 (2003) 133–141.
- [74] F. Acosta-Humánez, O. Almanza, C. Vargas-Hernández, Effect of sintering temperature on the structure and mean crystallite size of Zn<sub>1-x</sub>Co<sub>x</sub>O ( $x = 0.01-0.05$ ) samples, *Superf. Y. Vac. ío 27* (2014) 43–48.
- [75] M. Sun, B. Zhang, H. Liu, B. He, F. Ye, L. Yu, C. Sun, H. Wen, The effect of acid/alkali treatment on the catalytic combustion activity of manganese oxide octahedral molecular sieves, *RSC Adv.* 7 (2017) 3958–3965.
- [76] H. Zhang, S. Sui, X. Zheng, R. Cao, P. Zhang, One-pot synthesis of atomically dispersed Pt on MnO<sub>2</sub> for efficient catalytic decomposition of toluene at low temperatures, *Appl. Catal. B* 257 (2019), <https://doi.org/10.1016/j.apcatb.2019.117878>.
- [77] Y. Yin, W. Xu, S.L. Suib, C.L. O'Young, Lattice oxygen mobility and structural stability of Ni and Cu octahedral molecular sieves having the cryptomelane structure, *Inorg. Chem.* 34 (1995) 4187–4193.
- [78] J. Ye, M. Zhou, Y. Le, B. Cheng, J. Yu, Three-dimensional carbon foam supported MnO<sub>2</sub>/Pt for rapid capture and catalytic oxidation of formaldehyde at room temperature, *Appl. Catal. B* 267 (2020), <https://doi.org/10.1016/j.apcatb.2020.118689>.
- [79] P.M. Ette, K. Selvakumar, S.M. Senthil Kumar, K. Ramesha, Silica template assisted synthesis of ordered mesoporous  $\beta$ -MnO<sub>2</sub> nanostructures and their performance evaluation as negative electrode in Li-ion batteries, *Electro Acta* 292 (2018) 532–539, <https://doi.org/10.1016/j.electacta.2018.09.172>.
- [80] K. Selvakumar, S.M.S. Kumar, R. Thangamuthu, P. Rajput, D. Bhattacharyya, S. N. Jha, 2D and 3D Silica-Template-Derived MnO<sub>2</sub> Electrode catalysts towards enhanced oxygen evolution and oxygen reduction activity, *ChemElectroChem* 5 (2018) 3980–3990, <https://doi.org/10.1002/celec.201801143>.
- [81] C. Yu, L. Zhang, J. Shi, J. Zhao, J. Gao, D. Yan, A simple template-free strategy to synthesize nanoporous manganese and nickel oxides with narrow pore size distribution, and their electrochemical properties, *Adv. Funct. Mater.* 18 (2008) 1544–1554, <https://doi.org/10.1002/adfm.200701052>.
- [82] Z.Y. Leong, H.Y. Yang, A Study of MnO<sub>2</sub> with different crystalline forms for pseudocapacitive desalination, *ACS Appl. Mater. Interfaces* 11 (2019) 13176–13184, <https://doi.org/10.1021/acsami.8b20880>.
- [83] B. Ilhan, C. Annink, D.V. Nguyen, F. Mugele, I. Siretanu, M.H.G. Duits, A method for reversible control over nano-roughness of colloidal particles, *Colloids Surf. A Physicochem Eng. Asp.* 560 (2019) 50–58.
- [84] M. Christensen, J.T. Rasmussen, A.C. Simonsen, Roughness analysis of single nanoparticles applied to atomic force microscopy images of hydrated casein micelles, *Food Hydrocoll.* 45 (2015) 168–174.
- [85] X. Duan, T. Zhao, Z. Yang, B. Niu, G. Li, B. Li, Z. Zhang, J. Cheng, Z. Hao, Oxygen activation-boosted manganese oxide with unique interface for chlorobenzene oxidation: unveiling the roles and dynamic variation of active oxygen species in heterogeneous catalytic oxidation process, *Appl. Catal. B* 331 (2023) 122719.
- [86] F. Wang, Y. Zheng, Q. Chen, Z. Yan, D. Lan, E. Lester, T. Wu, A critical review of facets and defects in different MnO<sub>2</sub> crystalline phases and controlled synthesis—its properties and applications in the energy field, *Coord. Chem. Rev.* 500 (2024) 215537.
- [87] Q. Feng, H. Kanoh, K. Ooi, Manganese oxide porous crystals, *J. Mater. Chem.* 9 (1999) 319–333.
- [88] T. Brousse, M. Toupin, R. Dugas, L. Athouel, O. Crosnier, D. Belanger, Crystalline MnO<sub>2</sub> as possible alternatives to amorphous compounds in electrochemical supercapacitors, *J. Electrochem. Soc.* 153 (2006) A2171.
- [89] X. Wang, W. Tan, K. Guo, J. Ji, F. Gao, Q. Tong, L. Dong, Evaluation of manganese oxide octahedral molecular sieves for CO and C<sub>3</sub>H<sub>6</sub> oxidation at diesel exhaust conditions, *Frontiers in Environ. Chem.* 2 (2021) 672250.
- [90] X. Li, S. Ren, Z. Chen, M. Wang, L. Chen, H. Chen, X. Yin, A review of Mn-based catalysts for abating NO<sub>x</sub> and CO in low-temperature flue gas: performance and mechanisms, *Molecules* 28 (2023) 6885.
- [91] N.P.L. Magnard, A.S. Anker, O. Aalling-Frederiksen, A. Kirsch, K.M.Ø. Jensen, Characterisation of intergrowth in metal oxide materials using structure-mining: the case of  $\gamma$ -MnO<sub>2</sub>, *Dalton Trans.* 51 (2022) 17150–17161, <https://doi.org/10.1039/D2DT02153F>.
- [92] C. Julien, M. Massot, S. Rangan, M. Lemal, D. Guyomard, Study of structural defects in  $\gamma$ -MnO<sub>2</sub> by Raman spectroscopy, *J. Raman Spectrosc.* 33 (2002) 223–228, <https://doi.org/10.1002/jrs.838>.
- [93] A. Ramírez, P. Hillebrand, D. Stellmach, M.M. May, P. Bogdanoff, S. Fiechter, Evaluation of MnOx, Mn<sub>2</sub>O<sub>3</sub>, and Mn<sub>3</sub>O<sub>4</sub> electrodeposited films for the oxygen evolution reaction of water, *J. Phys. Chem. C* 118 (2014) 14073–14081, <https://doi.org/10.1021/jp500939d>.
- [94] Y. Yang, P. Zhang, K. Hu, P. Zhou, Y. Wang, A.H. Asif, X. Duan, H. Sun, S. Wang, Crystallinity and valence states of manganese oxides in Fenton-like polymerization of phenolic pollutants for carbon recycling against degradation, *Appl. Catal. B* 315 (2022) 121593, <https://doi.org/10.1016/j.apcatb.2022.121593>.
- [95] C. Cocuzza, E. Sartoretti, C. Novara, F. Giorgis, S. Bensaid, N. Russo, D. Fino, M. Piumetti, Copper-manganese oxide catalysts prepared by solution combustion synthesis for total oxidation of VOCs, *Catal. Today* 423 (2023) 114292, <https://doi.org/10.1016/j.cattod.2023.114292>.
- [96] T. Gao, H. Fjellvåg, P. Norby, A comparison study on Raman scattering properties of  $\alpha$ - and  $\beta$ -MnO<sub>2</sub>, *Anal. Chim. Acta* 648 (2009) 235–239, <https://doi.org/10.1016/j.aca.2009.06.059>.
- [97] F. Buciuman, F. Patcas, R. Craciun, D.R.T. Zahn, Vibrational spectroscopy of bulk and supported manganese oxides, *Phys. Chem. Chem. Phys.* 1 (1999) 185–190, <https://doi.org/10.1039/a807821a>.
- [98] R. Naeem, M. Ali Ehsan, R. Yahya, M. Sohail, H. Khaledi, M. Mazhar, Fabrication of pristine Mn<sub>2</sub>O<sub>3</sub> and Ag-Mn<sub>2</sub>O<sub>3</sub> composite thin films by AACVD for photoelectrochemical water splitting, *Dalton Trans.* 45 (2016) 14928–14939, <https://doi.org/10.1039/c6dt02656g>.
- [99] E.C. Njagi, H.C. Genuino, C.K. King'Ondu, S. Dharmarathna, S.L. Suib, Catalytic oxidation of ethylene at low temperatures using porous copper manganese oxides, *Appl. Catal. A Gen.* 421–422 (2012) 154–160, <https://doi.org/10.1016/j.apcata.2012.02.011>.
- [100] H. Zhang, X. Zheng, T. Xu, P. Zhang, Atomically dispersed Y or La on Birnessite-Type MnO<sub>2</sub> for the catalytic decomposition of low-concentration toluene at room temperature, *ACS Appl. Mater. Interfaces* 13 (2021) 17532–17542, <https://doi.org/10.1021/acsami.1c01433>.
- [101] C. Liu, J. Wang, J. Tian, L. Xiang, Synthesis and surface characterization of  $\gamma$ -MnO<sub>2</sub> nanostructures, *J. Nanomat.* 2013 (2013), <https://doi.org/10.1155/2013/389634>.
- [102] E. Sartoretti, C. Novara, A. Chiodoni, F. Giorgis, M. Piumetti, S. Bensaid, N. Russo, D. Fino, Nanostructured ceria-based catalysts doped with La and Nd: how acid-base sites and redox properties determine the oxidation mechanisms, *Catal. Today* 390 (2022) 117–134.
- [103] M. Piumetti, N. Russo, Notes on Catalysis for Environment and Energy, 2017.
- [104] S. Andreoli, F.A. Deorsola, C. Galletti, R. Pirone, Nanostructured MnOx catalysts for low-temperature NOx SCR, *Chem. Eng. J.* 278 (2015) 174–182.
- [105] S. Zhan, D. Zhu, M. Qiu, H. Yu, Y. Li, Highly efficient removal of NO with ordered mesoporous manganese oxide at low temperature, *RSC Adv.* 5 (2015) 29353–29361.
- [106] J. Yang, S. Ren, B. Su, Y. Zhou, G. Hu, L. Jiang, J. Cao, W. Liu, L. Yao, M. Kong, Insight into N<sub>2</sub>O formation over different crystal phases of MnO<sub>2</sub> during low-temperature NH<sub>3</sub>-SCR of NO, *Catal. Lett.* 151 (2021) 2964–2971.
- [107] F. Salomone, G. Bonura, F. Frusteri, M. Castellino, M. Fontana, A.M. Chiodoni, N. Russo, R. Pirone, S. Bensaid, Physico-chemical modifications affecting the activity and stability of Cu-based hybrid catalysts during the direct hydrogenation of carbon dioxide into dimethyl-ether, *Materials* 15 (2022), <https://doi.org/10.3390/ma15217774>.
- [108] H. Yang, C. Ma, X. Zhang, Y. Li, J. Cheng, Z. Hao, Understanding the active sites of Ag/zeolites and deactivation mechanism of ethylene catalytic oxidation at room temperature, *ACS Catal.* 8 (2018) 1248–1258.
- [109] F.X. Tian, M. Zhu, X. Liu, W. Tu, Y.F. Han, Dynamic structure of highly disordered manganese oxide catalysts for low-temperature CO oxidation, *J. Catal.* 401 (2021) 115–128, <https://doi.org/10.1016/j.jcat.2021.07.016>.
- [110] Z. Hu, R. Mi, X. Yong, S. Liu, D. Li, Y. Li, T. Zhang, Effect of crystal phase of MnO<sub>2</sub> with similar nanorod-shaped morphology on the catalytic performance of benzene combustion, *ChemistrySelect* 4 (2019) 473–480.
- [111] Z. Sibaib, F. Puleo, J.M. Garcia-Vargas, L. Retailleau, C. Descorme, L.F. Liotta, J. L. Valverde, S. Gil, A. Giroir-Fendler, Manganese oxide-based catalysts for toluene oxidation, *Appl. Catal. B* 209 (2017) 689–700, <https://doi.org/10.1016/j.apcatb.2017.03.042>.
- [112] M. Li, D.H. Wang, X.C. Shi, Z.T. Zhang, T.X. Dong, Kinetics of catalytic oxidation of CO over copper-manganese oxide catalyst, *Sep. Purif. Technol.* 57 (2007) 147–151, <https://doi.org/10.1016/j.seppur.2007.03.016>.
- [113] M. Baldi, V.S. Escrivano, J.M.G. Amores, F. Milella, G. Busca, Characterization of manganese and iron oxides as combustion catalysts for propane and propene,

- Appl. Catal. B 17 (1998) 175–182, [https://doi.org/10.1016/S0926-3373\(98\)00013-7](https://doi.org/10.1016/S0926-3373(98)00013-7).
- [114] D. Gu, J.C. Tseng, C. Weidenthaler, H.J. Bongard, B. Spliethoff, W. Schmidt, F. Soulamani, B.M. Weckhuysen, F. Schüth, Gold on different manganese oxides: ultra-low-temperature CO oxidation over colloidal gold supported on Bulk-MnO<sub>2</sub> Nanomaterials, *J. Am. Chem. Soc.* 138 (2016) 9572–9580, <https://doi.org/10.1021/jacs.6b04251>.
- [115] L. Pahalagedara, D.A. Kriz, N. Wasalathanthri, C. Weerakkody, Y. Meng, S. Dissanayake, M. Pahalagedara, Z. Luo, S.L. Suib, P. Nandi, R.J. Meyer, Benchmarking of manganese oxide materials with CO oxidation as catalysts for low temperature selective oxidation, *Appl. Catal. B* 204 (2017) 411–420, <https://doi.org/10.1016/j.apcatb.2016.11.043>.
- [116] J. Zhang, Y. Li, L. Wang, C. Zhang, H. He, Catalytic oxidation of formaldehyde over manganese oxides with different crystal structures, *Catal. Sci. Technol.* 5 (2015) 2305–2313, <https://doi.org/10.1039/c4cy01461h>.
- [117] C. He, Y. Wang, Z. Li, Y. Huang, Y. Liao, D. Xia, S. Lee, Facet Engineered  $\alpha$ -MnO<sub>2</sub> for Efficient Catalytic Ozonation of Odor CH<sub>3</sub>SH: oxygen vacancy-induced active centers and catalytic mechanism, *Environ. Sci. Technol.* 54 (2020) 12771–12783, <https://doi.org/10.1021/acs.est.0c05235>.
- [118] K. Li, J. Chen, Y. Peng, W. Lin, T. Yan, J. Li, The relationship between surface open cells of  $\alpha$ -MnO<sub>2</sub> and CO oxidation ability from a surface point of view, *J. Mater. Chem. A Mater.* 5 (2017) 20911–20921, <https://doi.org/10.1039/c7ta04624c>.
- [119] J. Huang, S. Zhong, Y. Dai, C.C. Liu, H. Zhang, Effect of MnO<sub>2</sub> phase structure on the oxidative reactivity toward bisphenol A Degradation, *Environ. Sci. Technol.* 52 (2018) 11309–11318, <https://doi.org/10.1021/acs.est.8b03383>.
- [120] B. Zhao, R. Ran, X. Wu, D. Weng, Phase structures, morphologies, and NO catalytic oxidation activities of single-phase MnO<sub>2</sub> catalysts, *Appl. Catal. A Gen.* 514 (2016), <https://doi.org/10.1016/j.apcata.2016.01.005>.
- [121] S. Rong, P. Zhang, F. Liu, Y. Yang, Engineering crystal facet of  $\alpha$ -MnO<sub>2</sub> nanowire for highly efficient catalytic oxidation of carcinogenic airborne formaldehyde, *ACS Catal.* 8 (2018) 3435–3446.
- [122] X.J. Zhou, Y. Sun, B. Zhu, J. Chen, J. Xu, H. Yu, M. Xu, Influencing mechanism of alkali metals on the adsorption property of NH<sub>3</sub>, NO, O<sub>2</sub> and dehydrogenation reaction of NH<sub>3</sub> on the  $\beta$ -MnO<sub>2</sub> (1 1 0) surface: A DFT+ U study, *Fuel* 318 (2022) 123470.
- [123] L. Zhang, S. Wang, L. Lv, Y. Ding, D. Tian, S. Wang, Insights into the reactive and deactivation mechanisms of manganese oxides for ozone elimination: the roles of surface oxygen species, *Langmuir* 37 (2021) 1410–1419.
- [124] J. Huang, R. Fang, Y. Sun, J. Li, F. Dong, Efficient  $\alpha$ -MnO<sub>2</sub> with (2 1 0) facet exposed for catalytic oxidation of toluene at low temperature: a combined in-situ DRIFTS and theoretical investigation, *Chemosphere* 263 (2021) 128103.
- [125] W. Li, X. Cui, R. Zeng, G. Du, Z. Sun, R. Zheng, S.P. Ringer, S.X. Dou, Performance modulation of  $\alpha$ -MnO<sub>2</sub> nanowires by crystal facet engineering, *Sci. Rep.* 5 (2015) 8987.
- [126] D. Su, H.-J. Ahn, G. Wang,  $\beta$ -MnO<sub>2</sub> nanorods with exposed tunnel structures as high-performance cathode materials for sodium-ion batteries, *NPG Asia Mater.* 5 (2013) e70–e70.
- [127] D. Fang, F. He, D. Li, J. Xie, First principles and experimental study of NH<sub>3</sub> adsorptions on MnO<sub>x</sub> surface, *Appl. Surf. Sci.* 285 (2013) 215–219.
- [128] W. Yang, Y. Peng, Y. Wang, Y. Wang, H. Liu, Z. Su, W. Yang, J. Chen, W. Si, J. Li, Controllable redox-induced in-situ growth of MnO<sub>2</sub> over Mn<sub>2</sub>O<sub>3</sub> for toluene oxidation: active heterostructure interfaces, *Appl. Catal. B* 278 (2020) 119279.